

Dynamics of spin-momentum entanglement from superradiant phase transitions

Oksana Chelpanova¹,¹ Kushal Seetharam^{2,3},^{2,3} Rodrigo Rosa-Medina⁴,⁴
 Nicola Reiter⁴,⁴ Fabian Finger⁴,⁴ Tobias Donner⁴,⁴ and Jamir Marino¹

¹*Institut für Physik, Johannes Gutenberg-Universität Mainz, D-55099 Mainz, Deutschland*

²*Department of Electrical Engineering, Massachusetts Institute of Technologies, Cambridge, Massachusetts 02139, USA*

³*Department of Physics, Harvard University, Cambridge MA, 02138, USA*

⁴*Institute for Quantum Electronics, ETH Zürich, 8093 Zürich, Switzerland*

(Dated: June 28, 2024)

Exploring operational regimes of many-body cavity QED with multi-level atoms remains an exciting research frontier for their enhanced storage capabilities of intra-level quantum correlations. In this work, we consider an experimentally feasible many-body cavity QED model describing a four-level system, where each of those levels is formed from a combination of different spin and momentum states of ultra-cold atoms in a cavity. The resulting model comprises a pair of Dicke Hamiltonians constructed from pseudo-spin operators, effectively capturing two intertwined superradiant phase transitions. The phase diagram reveals regions featuring weak and strong entangled states of spin and momentum atomic degrees of freedom. These states exhibit different dynamical responses, ranging from slow to fast relaxation, with the added option of persistent entanglement temporal oscillations. We discuss the role of cavity losses in steering the system's dynamics into such entangled states and propose a readout scheme that leverages different light polarizations within the cavity. Our work paves the way to connect the rich variety of non-equilibrium phase transitions that occur in many-body cavity QED to the buildup of quantum correlations in systems with multi-level atom descriptions.

I. INTRODUCTION

The coupling between spin and motional degrees of freedom lies at the root of several rich phenomena in quantum physics, including fine structure splitting of atoms [1] and the spin Hall effect [2], which, in turn, allow the realization of topological phases of matter [3, 4] and open the possibility of topological quantum computing [5, 6]. Spin-momentum entanglement resulting from such coupling has increasingly become relevant in a variety of research areas, ranging from materials science to photonics and atomic systems [7–9]. In this work, we propose a protocol for engineering entanglement between the spin and momentum degrees of freedom of ultracold atoms coupled to an optical cavity. Our approach exploits a non-equilibrium superradiant phase transition in the system realized by coupling four atomic modes, which comprise two internal (spin) and external (momentum) states of the atom.

Many-body cavity QED experiments with ultracold atoms are among the most versatile quantum simulators of driven-dissipative phases of matter [10]. The combination of tunable photon-mediated long-range interatomic interactions, along with strong cooperative effects and control on cavity losses, offers a wide range of possibilities, encompassing non-equilibrium transitions [11–20], dynamical control of correlations [21–26], realization of dark states [27–29], and the exploration of collective phenomena purely driven by engineered dissipation [30–32]. Oftentimes, the effective atomic degrees of freedom in state-of-art experiments are a pair of momentum states or internal levels, optically addressed by external laser drives inducing cavity-assisted two-photon transitions [12, 33–35]. Recently, a few cavity QED ex-

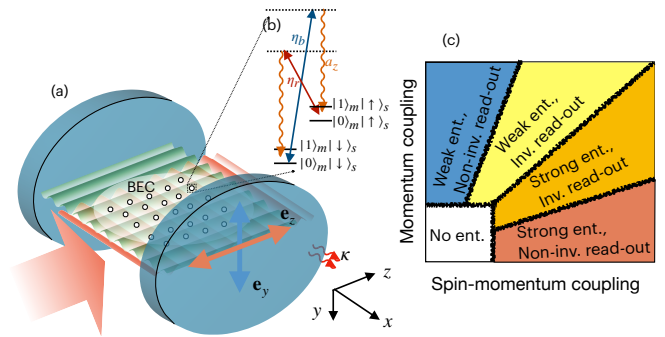


FIG. 1. (a) Sketch of the cavity QED setup and (b) of the atomic level scheme. (c) Cartoon of the dynamical phase diagram as a function of the couplings between spin and momentum degrees of freedom.

periments and theory works have shown how to couple the momentum and internal spin degrees of freedom of ultracold atoms using intra-cavity light, demonstrating novel self-organized phases [11, 36–39].

In this paper, we generalize such protocols to show that spin-momentum entanglement can be synthesized, controlled, and steered in experiments by coupling motional and internal degrees of freedom. We consider a cavity QED platform, cf. Fig. 1(a), which is described by a minimal model with two different spin states and two different momentum states, meaning that each atom can occupy one of these four hybrid spin-momentum states shown in Fig. 1(b). We demonstrate that this system exhibits superradiant phase transitions related to the self-organization of the atoms in the cavity, concomitantly with the dynamical buildup of spin-momentum entanglement. By varying the spin-momentum coupling, one

can robustly tune the entanglement up to its maximum possible value.

The superradiant phase transitions within this model exhibit notable distinctions from the conventional phenomenology of self-organization in cavity QED [11, 12, 31–33, 40–44]. While the hybrid spin-momentum order parameter in our system and the photon number approach stationary values, the spin and momentum separately can be non-stationary. This results in a time-dependent profile of the condensate density and the effective spin magnetization, which is unconventional for state-of-art cavity QED experiments [36, 37]. Such oscillations persist beyond the operational time scales of these platforms, resulting in long-lived non-stationary dynamical responses. We show that such features can be continuously probed using an auxiliary cavity field, which is coupled to the momentum degree of freedom of atoms. The overall dynamics in such a model are conditioned by the intertwining of two cavity-mediated processes, controlled by two couplings between momentum states or hybrid momentum-spin states. The different dynamical responses of the system, summarized in Fig. 1(c), are characterized by weak or strong entanglement. In particular, despite the back-action and intrinsic decoherence of the read-out process, proxy of spin-momentum entanglement dynamics can be non-invasively accessed in an extended parameter regime [red region in Fig. 1(c)], making the system a possible candidate for quantum information applications [45].

Crucially, in our scheme, cavity losses have the beneficial role of steering dynamics towards target entangled states, thereby endowing robustness to the initial condition of the system. This feature is absent in protocols engineering spin-momentum entanglement in BECs using solely classical drive fields [8]. In such proposals, the degree of achievable spin-momentum entanglement is highly sensitive with respect to technical fluctuations of different experimental parameters (e.g., drive powers and frequencies). In contrast, protocols relying on cavity losses induce contractive dynamics which are insensitive to such issues and initial state preparation, therefore offering a more robust and reliable route for spin-momentum entanglement generation.

A. Outline of the article

The paper is organized as follows. In Sec. II, we present an experimentally motivated effective model that governs the dynamics of the cavity QED setup in Fig. 1, where the spin and momentum of atoms are coupled to the cavity field. Sec. III is devoted to the superradiant phase transition and subsequent generation of entanglement between spin and momentum degrees of freedom. In Sec. IV, we extend the model by introducing an auxiliary cavity mode and show how it enables continuous read-out of the system dynamics. In Sec. V, we analyze the dynamical responses and read-out strategies. In Sec. VI, we revisit

entanglement generation in the presence of the auxiliary cavity mode and discuss prospects for its non-invasive read-out. In the concluding Section VII, we summarize our findings and discuss follow-up directions.

II. MODEL

We consider a cavity QED configuration in which we can address both the spin and momentum states of ultracold atoms, enabling measurement and dynamic control (see also Ref. [36] for a related setup). Specifically, we consider Bose-Einstein condensate (BEC) of ^{87}Rb atoms in the $F = 1$ hyperfine ground state manifold confined in a high-finesse optical cavity. The atoms are coupled to a z -polarized cavity mode a_z with resonance frequency ω_c and decay rate κ , extending along x direction, as illustrated in Fig. 2(a). A bias magnetic field \vec{B} along the z direction defines the quantization axis and induces Zeeman splitting between the sub-levels of the $F = 1$ hyperfine manifold. We focus on two internal atomic sub-levels $|m_F = 1\rangle = |\downarrow\rangle_s$ and $|m_F = 0\rangle = |\uparrow\rangle_s$, and describe the condensate with the spinor wave function $\Psi = (\psi_\uparrow, \psi_\downarrow)^T$.

The condensate is illuminated with transverse standing-wave laser fields far-detuned from the electronic transitions of the atoms. These detunings allow us to effectively eliminate the contribution of excited electronic states and to focus on the near-resonant cavity-assisted two-photon transitions between an atomic momentum state $|0\rangle_m = |k_x = 0, k_z = 0\rangle$ and an excited one, which reads as a coherent superposition $|1\rangle_m = \sum_{s,s'=\pm} |k_x = sk, k_z = s'k\rangle/2$. Here, $\hbar k = 2\pi\hbar/\lambda$ indicates the recoil momentum, with $\lambda/2 = 784.7/2$ nm representing the period of the standing-wave potential along the drive direction.

We introduce the following definitions of relevant combinations of momentum and spin states [cf. Fig. 2(b)]

$$\begin{aligned} |0\rangle &= |0\rangle_m \otimes |\downarrow\rangle_s, \\ |1\rangle &= |1\rangle_m \otimes |\downarrow\rangle_s, \\ |2\rangle &= |0\rangle_m \otimes |\uparrow\rangle_s, \\ |3\rangle &= |1\rangle_m \otimes |\uparrow\rangle_s, \end{aligned} \tag{1}$$

limiting our consideration to a four-level model of the system, which will be further justified in the following. In this notation, even states $|0\rangle$ and $|2\rangle$ are momentum ground states that correspond to the homogeneous condensate density in real space, while odd states $|1\rangle$ and $|3\rangle$ are excited momentum states and correspond to a modulation of the atomic density in real space: $|1\rangle_m \propto \cos kx \cos kz$ (see also Ref. [12]). We also introduce boson annihilation and creation operators $c_{0,\dots,3}$, $c_{0,\dots,3}^\dagger$, $[c_i, c_j^\dagger] = \delta_{i,j}$, which describe the annihilation and creation of a particle in these four state manifold of Eqs. (1).

We consider Raman processes that simultaneously couple internal (spin) and external (momentum) atomic de-

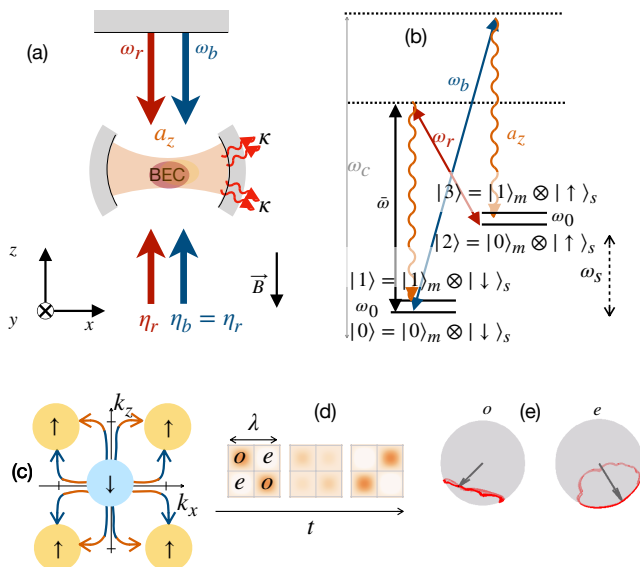


FIG. 2. (a) Schematics of the experimental setup and (b) corresponding level scheme for the model (2). (c) Momentum space cartoon for spin-flipping Raman process for a transition $|0\rangle \rightarrow |3\rangle$; (d) Snapshots of the real-space BEC density in the $|\uparrow\rangle_s$ manifold at different times; (e) Dynamics in the superradiant phase of the spin components on even (e) and odd (o) lattice sites plotted on the Bloch spheres.

degrees of freedom [36, 37, 46]. These processes are mediated by the interaction of the cavity mode a_z and two classical driving fields with coupling strength $\eta_b = \eta_r = \eta$ and frequencies ω_b, ω_r , with $2\bar{\omega} = \omega_b + \omega_r$, $\delta = \omega_b - \omega_r$. In this context, the laser at frequency ω_b facilitates the transition between states $|0\rangle$ and $|3\rangle$, from the ground momentum state $|0\rangle_m$ to the excited momentum state $|1\rangle_m$, accompanied by a spin flip from $|\downarrow\rangle_s$ to $|\uparrow\rangle_s$ and vice versa. Conversely, the laser at frequency ω_r induces a similar transition, $|2\rangle \leftrightarrow |1\rangle$, accompanied by a spin flip from $|\uparrow\rangle_s$ to $|\downarrow\rangle_s$, cf. Fig. 2(b,c). These two cavity-assisted Raman processes mediate an interaction of the form $\eta(a_z + a_z^\dagger) \cos kx \cos kz (F^+ + F^-)$, where the spin operators F^\pm couple neighboring spin levels [cf. momentum cartoon in Fig. 2(c) and Appendix A for the model details]. After integrating over the spatial extent of the condensate, the Hamiltonian of the effective model reads

$$H = \omega_z a_z^\dagger a_z + (\omega_0 - \omega_s) S_{12}^z + (\omega_0 + \omega_s) S_{03}^z + 2\eta(a_z + a_z^\dagger)(S_{12}^x + S_{03}^x), \quad (2)$$

where ω_z is the cavity detuning (cf. Appendix A), ω_0 is the double recoil energy $\omega_{\text{rec}} = k^2/(2M)$, which atoms acquire in the two-photon process, and ω_s is the effective splitting between the two spin manifolds. We set $\hbar = 1$ to keep the notation compact.

The cavity boson field a_z satisfies the commutation relations $[a_z, a_z] = 0$, $[a_z, a_z^\dagger] = 1$. The collective pseudo-spin operators S are built as projectors between the macroscopically occupied spin-momentum levels $S_{ij}^- = |i\rangle\langle j| = c_i^\dagger c_j$, $S_{ij}^+ = (S_{ij}^-)^\dagger$, $S_{ij}^z = (c_j^\dagger c_j - c_i^\dagger c_i)/2$, $S_{ij}^x =$

$(S_{ij}^- + S_{ij}^+)/2$ with $(i, j) \in \{(0, 3), (1, 2)\}$ for $i = 0, \dots, 3 < j$. Here, we already rescaled spin and photon operators via $S \rightarrow S/N$, $a_z \rightarrow a_z/\sqrt{N}$ (and also $c_i \rightarrow c_i/\sqrt{N}$) as it is convenient for collective spin models [44, 47], where N is a number of atoms in the condensate. Similarly, one can introduce other pseudo-spin operators \mathcal{T} , that are built from different spin states of the same momentum: $\mathcal{T}_{ij}^- = c_i^\dagger c_j, \dots$ where $(i, j) \in \{(0, 2), (1, 3)\}$, or when $(i, j) \in \{(0, 1), (2, 3)\}$ pseudo-spin operators $J_{ij}^- = c_i^\dagger c_j$ correspond to transitions between different momentum states of the same internal spin.

The dynamics of the system are described by the Lindblad master equation for the density matrix ρ

$$\begin{aligned} \frac{d}{dt}\rho &= -i[H, \rho] + \kappa\mathcal{D}(\rho) \\ \mathcal{D}(\rho) &= 2a_z\rho a_z^\dagger - \{a_z^\dagger a_z, \rho\}. \end{aligned} \quad (3)$$

where cavity losses account for the finite lifetime $\propto 1/\kappa$ of the cavity photon a_z .

Our proposal is inspired by the experiments reported in Refs. [11, 36] that typically involve a substantial number of atoms, around $N \approx 10^4 - 10^5$, and deviations from mean-field behavior only become pronounced at extremely long timescales. The coupling between photons and atoms is collective [cf. Eq. (2)], and results in a suppression of light-matter correlations by a factor of $1/N$. The dynamics are thus well captured by mean-field equations of motion, which we report in Appendix B for completeness. However, correlations between the spin and momentum degrees of freedom within the condensate play a significant role in entanglement dynamics, as we show in detail in the following Section.

The dynamics in Eq. (3) possess a \mathbb{Z}_2 symmetry characteristic of Dicke models [33, 36, 37, 48, 49]: it is invariant under the transformation $(a_z, S^x) \leftrightarrow (-a_z, -S^x)$, where $S^x = S_{03}^x + S_{12}^x$ [cf. Eq. (2)]. When this symmetry is spontaneously broken, the system undergoes a phase transition. In the thermodynamic limit, the transition can shift the system from the trivial normal state with the empty cavity mode $n_z = \langle a_z^\dagger a_z \rangle = |\langle a_z \rangle|^2 = 0$ and all spins polarized along the z direction to the superradiant (SR) phase with the non-zero occupation of the cavity mode and finite x component of the spin, namely $n_z \neq 0$ and $\langle S^x \rangle \neq 0$ (cf. Appendix D or Ref. [44] for more details). Throughout this paper, we employ $\langle \cdot \rangle$ to denote expectation values of observables.

When $\omega_s = 0$, the critical coupling at which the transition to the SR phase takes place read $\eta_{\omega_s=0}^c = [\omega_0(\omega_z^2 + \kappa^2)/(4\omega_z)]^{1/2}$ [48, 50], while for $\omega_s \neq 0$ case, the critical coupling becomes sensitive to the initial conditions. This sensitivity is rooted in the different effective level splitting for pseudo-spins S_{03} and S_{12} , $\omega_0 \pm \omega_s$. The specific distribution of particles between the two pseudo-spins, S_{03} and S_{12} , gives rise to distinct effective level splittings between excited and ground momentum states, and thus different critical couplings. A similar dependence on the initial state also emerges when

there is disorder in the coupling constants, as discussed in Refs. [51, 52].

To illustrate this dependence, consider initialization of the system in a mixture of the atoms in the ground momentum state, $|k_x, k_z\rangle = |0\rangle_m$, with two different magnetic numbers; namely, we prepare $N_0 = N\langle c_0^\dagger c_0\rangle = \mu N$ particles in level $|0\rangle$ and $N_2 = N\langle c_2^\dagger c_2\rangle = (1 - \mu)N$ particles in level $|2\rangle$, where $\mu \in [0, 1]$. This results in the critical coupling (see Appendix D)

$$2\eta^c = \begin{cases} \sqrt{\frac{(\omega_0^2 - \omega_s^2)(\omega_z^2 + \kappa^2)/\omega_z}{(\omega_s + \omega_0) - 2\mu\omega_s}}, & \omega_s < \omega_0 \\ \sqrt{\frac{(\omega_s^2 - \omega_0^2)(\omega_z^2 + \kappa^2)/\omega_z}{(\omega_s + \omega_0) - 2\mu\omega_0}}, & \omega_s > \omega_0. \end{cases} \quad (4)$$

If the system is prepared in the spin-polarized state, the expression for the critical coupling simplifies to $2\eta_c = [(\omega_0 \pm \omega_s)(\omega_z^2 + \kappa^2)/\omega_z]^{1/2}$ for $\mu = 0, 1$, coinciding with the critical coupling in Ref. [53].

In order to study the onset of the SR phase on a microscopic level, we evaluate the condensate $|\psi_{\uparrow, \downarrow}\rangle^2$ and the spin $\Psi^\dagger \sigma_i \Psi / 2$ densities. Here, we use spin-1/2 Pauli matrices σ_i instead of spin operators F of the original problem to highlight the two-level internal spin structure of the effective model. The spinor $\Psi = (\psi_\uparrow, \psi_\downarrow)^T$ has components $\psi_\downarrow = \langle c_0\rangle + \langle c_1\rangle \cos kx \cos kz$, and $\psi_\uparrow = \langle c_2\rangle + \langle c_3\rangle \cos kx \cos kz$, cf. Appendix A.

When $\mu \in (0, 1)$, both spin and condensate density are time dependent. We show a few snapshots of the condensate density at different times in Fig. 2(d) along with the spin for even and odd sites [Fig. 2(e)]; spin components are evaluated in the center of lattice cells of the size $\lambda/2 \times \lambda/2$. We explain such time-dependence from the fact that the correct order parameter that captures transition to the superradiant phase is the spin density integrated over the space, $\int d\mathbf{r} \Psi^\dagger \sigma^x \Psi \cos kx \cos kz$ (see derivation of the Hamiltonian in Appendix A). On the other hand, the x component of spatial spin profile (spin density) contains a time-independent contribution $\propto \text{Re}(\langle c_0^\dagger c_3\rangle + \langle c_2^\dagger c_1\rangle) \cos kx \cos kz \propto (\langle S_{03}^x\rangle + \langle S_{12}^x\rangle) \cos kx \cos kz$, which exactly reflects spontaneous breaking of the \mathbb{Z}_2 symmetry, and a time-dependent contribution of the form $\propto \text{Re}(\langle c_2^\dagger c_0\rangle + \langle c_3^\dagger c_1\rangle) \cos^2 kx \cos^2 kz \propto (\langle \mathcal{T}_{02}^x\rangle + \langle \mathcal{T}_{13}^x\rangle \cos^2 kx \cos^2 kz)$. Here, both $\langle \mathcal{T}^x(t)\rangle \propto \cos(\Omega t)$ [cf. expression for Ω in Appendix D] and are zero only if $\mu = 0$ or $\mu = 1$ (this particular case has been studied in [36, 37]). Such precession of $\langle \mathcal{T}\rangle$ originates from the fact that pseudo-spin species S , \mathcal{T} and J are built as bilinears of the same boson operators c_0, \dots, c_3 . Similarly, the total density $|\psi_\downarrow|^2 + |\psi_\uparrow|^2$ contains time-dependent contribution of the form $(\langle c_0^\dagger c_1\rangle + \langle c_2^\dagger c_3\rangle + \langle c_1^\dagger c_0\rangle + \langle c_3^\dagger c_2\rangle) \cos kx \cos kz \propto (\langle J_{01}^x\rangle + \langle J_{23}^x\rangle) \cos kx \cos kz$ which vanishes only if $\mu = 0, 1$. Otherwise, the spin and density distribution along the lattice are time-dependent. In the following section, we show the impact of such time dependence on the dynamics of entanglement between spin and momentum degrees of freedom.

Following experiments in Refs. [11, 36], we maintain the key parameters $\omega_0/(2\pi) \approx 7.4\text{kHz}$ and $\kappa/(2\pi) = 1.25\text{MHz}$ fixed for all simulations. The remaining detunings and coupling strengths are tunable, allowing for the exploration of a broad spectrum of dynamical regimes.

III. SPIN-MOMENTUM ENTANGLEMENT AND SUPERRADIANT DYNAMICS

Although correlations among different atoms are negligible, our platform offers a route to engineer robust entanglement between spin and momentum degrees of freedom within the bosonic condensate trapped in the cavity. For instance, assume all atoms are initially prepared in the state $|0\rangle = |0\rangle_m \otimes |\downarrow\rangle_s$. Through the interaction with the cavity mode a_z , the atoms are coupled to the state $|3\rangle = |1\rangle_m \otimes |\uparrow\rangle_s$ as $2\eta(a_z + a_z^\dagger)S_{03}^x|0\rangle = \eta(a_z + a_z^\dagger)|3\rangle$. Thus, in the SR phase with the non-zero cavity field ($\langle a_z\rangle \neq 0$), the cavity-mediated interaction gives rise to a non-separable spin-momentum state. The corresponding state of each atom reads

$$|\psi\rangle = \langle c_0\rangle|0\rangle_m \otimes |\downarrow\rangle_s + \langle c_3\rangle|1\rangle_m \otimes |\uparrow\rangle_s, \quad (5)$$

with $\langle c_0\rangle \neq 0$ and $\langle c_3\rangle \neq 0$, and $|\psi\rangle$ is a non-separable entangled state of spin and momentum. Our results will revolve around the dynamical manipulation of this form of entanglement.

In order to quantify spin-momentum entanglement, we use the von Neumann entropy

$$S_{\text{vN}} = -\text{Tr}(\tilde{\rho} \log_2 \tilde{\rho}) \quad (6)$$

with $\tilde{\rho}$ the reduced density matrix after tracing out spin or momentum states, cf. Appendix E. When the system is in a product state of spin and momentum, the entanglement vanishes and $S_{\text{vN}} = 0$. With the definition in Eq. (6), a maximally entangled state has $S_{\text{vN}} = 1$. We also compute negativity [54] and concurrence [55, 56], which are more reliable witnesses of entanglement in open systems [57]. However, they show the same qualitative behavior as S_{vN} (cf. Appendix E), and thus we restrict our analysis to the von Neumann entropy for its simplicity.

By adjusting coupling η and the initial state of atoms, we compute a dynamical phase diagram, which captures maximal S_{vN} reached during evolution, see Fig. 3. The system is initially prepared in the normal state with $N_0 = \mu N$ atoms in the state $|0\rangle$, after which we rapidly increase the coupling η to a specified value. The equations of motion describing this process can be found in Appendices B and C. Note that the collective description of the model, adapted in this work, is valid only when the system is prepared in the permutation invariant state; otherwise, dynamics become more complicated as discussed in [58–61]. Below, we analyze the entanglement properties for both the degenerate case ($\omega_s = 0$) and the non-degenerate case ($\omega_s \neq 0$), showcasing the

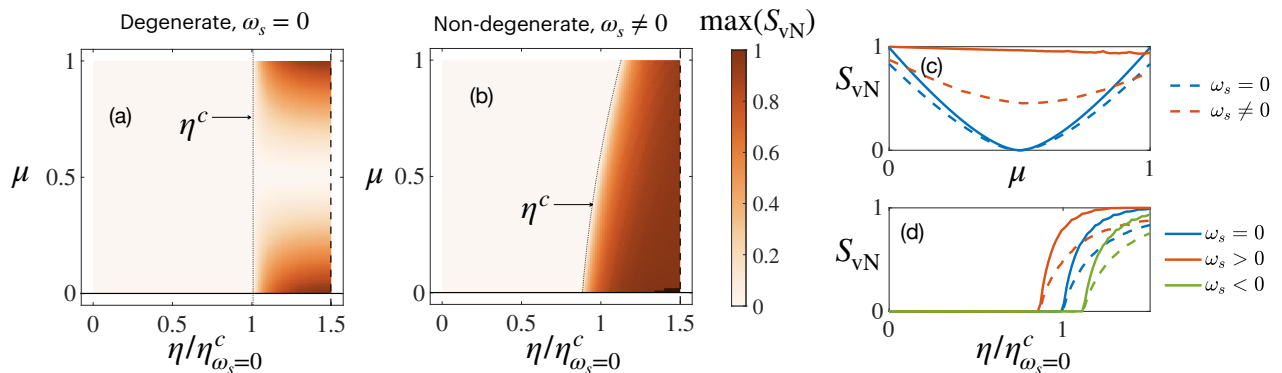


FIG. 3. (a-b) Maximum of spin-momentum entanglement S_{vN} as a function of $\eta/\eta_{\omega_s=0}^c$ and μ . Entanglement is built up as we enter the superradiant phase. Here (a) $\omega_s = 0$ and (b) $\omega_s = \omega_0/4$. (c) Maximal (solid lines) and time-averaged (dashed lines) entanglement entropy as a function of μ for different values of ω_s and $\eta/\eta_{\omega_s=0}^c = 1.5$. (d) Maximal (solid lines) and time-averaged (dashed lines) entanglement entropy as a function of photon-matter coupling η for $\mu = 0$. Different colors indicate different ω_s .

potential for achieving either a stationary or a time oscillating amount of entanglement, respectively.

1. Degenerate $\omega_s = 0$ case

The amount of S_{vN} reached during dynamics in the degenerate case is shown in Fig. 3(a). Depending on the initial configuration, the maximum amount of entanglement in the system can vary from $\max(S_{vN}) = 0$ to $\max(S_{vN}) = 1$. Specifically, when $\mu = 0.5$, the momentum configuration of each spin component reads exactly the same, and the state becomes separable. Conversely, when $\mu = 0$ or 1 , one can reach a maximally entangled state; the dependence of the entanglement in the system as a function of μ is shown with blue lines in Fig. 3(c). On the other hand, the amount of entanglement in the SR phase depends on the coupling η , [cf. dependence of the entanglement entropy as a function of coupling for $\mu = 0$ in panel (d), blue lines]. Here, entanglement increases with the coupling which can be qualitatively understood as follows. When $\eta \approx \eta^c$, almost all atoms occupy the ground momentum state and $|\psi\rangle \propto |2\rangle$, which is separable in terms of spin and momentum. However, as we increase coupling, the population of the excited momentum level $|1\rangle$ increases and the spin-momentum state of the system becomes non-separable, approaching a maximally entangled state deep in the SR phase. Importantly, by solving the dynamics of the system without cutting off the higher momentum state, we check that for large couplings, most of the atoms occupy momentum states $|0\rangle_m, |1\rangle_m$. The states $|0, 2k\rangle$ and $|2k, 0\rangle$ are significantly less populated during the dynamics, and we can neglect them. The corresponding equations of motion are given in Appendix B.

2. Non-degenerate $\omega_s \neq 0$ case

When $\omega_s \neq 0$, the dynamical behavior of the entanglement entropy changes compared to the degenerate case [see Fig. 3(b)]. First, the critical coupling depends on μ , cf. Eq. (4). Second, when $\mu = 0.5$, entanglement decreases but does not disappear completely [red lines in panel (c)]. Here, one can notice the difference between the maximal value of the entanglement (dashed line) and the period-averaged value (solid line), indicating an oscillatory behavior in time. The exceptional case is $\mu = 0, 1$ where the system evolves towards a stationary SR state. From the standpoint of spin-momentum correlations, this state has maximum (non-oscillatory) entanglement when compared with occurrences at other values of μ .

Fig. 4 depicts the dynamics of the entanglement entropy in the non-degenerate case after the quench during the period (a), along with the (b) occupation of the cavity field n_z and (c-d) spin (arrows) and density distributions of atoms. In panels (c-d) with arrows, we plot the projection of this spin density on the xz plane, evaluated in the center of each lattice cell of size $\lambda/2 \times \lambda/2$, which is formed by the interference of the laser and cavity fields.

In Fig. 4, maximally entangled configurations correspond to the case when the checkerboard lattice is formed by the spin degree of freedom (arrows), while the condensate density is periodically modulated with the period $\lambda/2$. On the contrary, in the configuration with vanishing entanglement, the sign of the spin projection $\Psi\sigma^x\Psi$ is fixed for all lattice cells, and the condensate density modulation occurs with a period λ . Such dynamics persist in time without any sign of relaxation [see Appendices B and D for more details].

Such dynamical behavior emerges from the time-dependent components of spin and condensate densities, if the system is initialized in the mixed internal spin state. While the total atom number $\int d\mathbf{r}|\Psi|^2 = N$, and transverse magnetization $\int d\mathbf{r}\Psi^\dagger\sigma^x\Psi/N \propto \langle S^x \rangle$, are con-

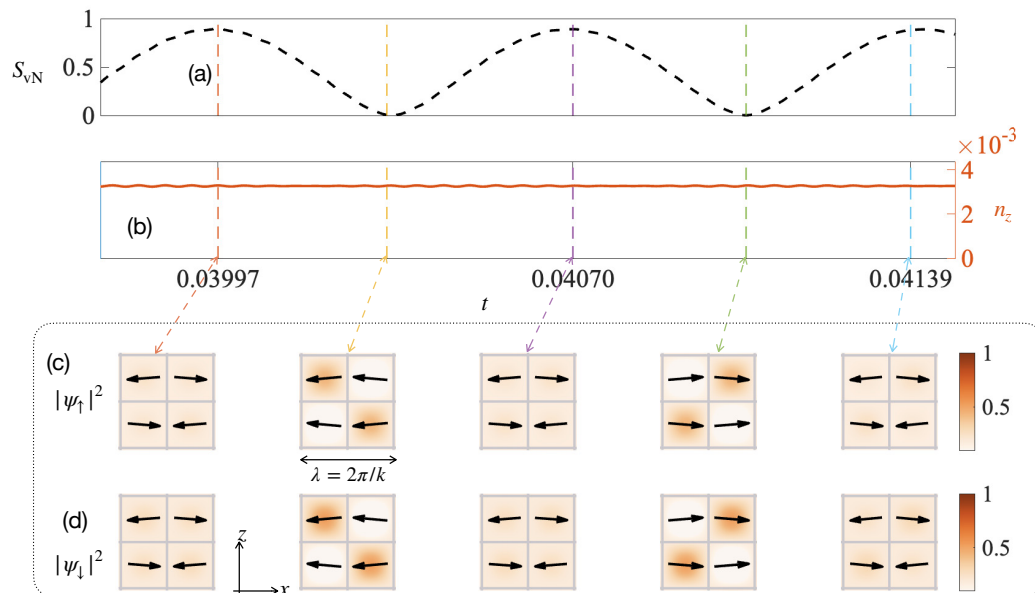


FIG. 4. (a) Dynamics of entanglement, (b) occupation of the cavity mode a_z , $n_z = \langle a_z^\dagger a_z \rangle$, density of the (c) upper $|\psi_\uparrow|^2$ and (d) lower $|\psi_\downarrow|^2$ spinor components. Black arrows in panels (c-d) indicate local spin texture $\Psi^\dagger \sigma_i \Psi / 2$, evaluated in the centers of each cell and projected onto the xz plane. Dashed lines indicate time moments when the entropy takes extremum values and is added to guide the eye. Entropy is maximized when the state $|\psi\rangle$ is a non-separable combination of two spin-momentum states, and SR manifests as a spin checkerboard lattice, i.e., projection of spin onto x axis takes opposite signs on even and odd lattice cells. When entanglement vanishes, both spinor components have similar density profiles and the sign of projection of the spin magnetization onto the x axis. Dynamics are simulated for $\mu = 0.5$, $\eta = 1.6\eta^c$, $\omega_s = \omega_0/4$, $\omega_z = \kappa$.

served quantities in the steady state, their local distributions can exhibit complicated time-dependence, driven by the precession of pseudo-spins $\langle J \rangle$ and $\langle \mathcal{T} \rangle$: When $\langle J^x \rangle$ and $\langle \mathcal{T}^x \rangle$ reach zero, the local distribution of spin and condensate densities are identical to the one obtained starting from the polarized spin state, and the entanglement entropy becomes maximal. When $\langle J^x \rangle$ and $\langle \mathcal{T}^x \rangle$ deviate from zero, the distribution of atoms among space and spin levels changes, decreasing the entanglement entropy. Thus, the time dependence of spin and momentum states results in oscillations of the entanglement entropy. This is one of the striking features of our quench protocol: we can steer entanglement dynamics toward an oscillatory regime that persists up to the operational timescales of the experiment.

Notice that entanglement is generated during dynamics starting from product spin-momentum states, and thus, the cavity photon has an active role in building spin-momentum correlations via light-induced interactions. The non-zero cavity field $\langle a_z \rangle$ in the SR phase mediates an effective interaction among atoms, which is responsible for entangling them in a non-separable spin-momentum state. At the same time, the role of cavity losses is essential. They steer dynamics towards the fixed point of the Lindbladian, with the remarkable consequence that all entanglement properties derived in the presence of photon losses are robust if compared with

what would be achieved with a coherent drive [8, 62, 63]. For instance, by replacing the cavity field with a time-dependent drive in H [Eq. (2)], one could also entangle spin and momentum degrees of freedom of the condensate's atoms. However, the amount of final entanglement produced would depend on details of the driving protocol, such as its duration, frequency decomposition, and other specifics. More importantly, such entanglement would be highly sensitive to noise and imperfections in the drive realization [64–66]. In contrast, cavity losses induce relaxation of atomic entanglement towards a steady state that remains resilient even for moderate imperfections in the initial state preparation or in the parameters set to drive dynamics into superradiance. In other words, there exists a broad basin of attraction towards prescribed values of entanglement given the system's initial conditions parameters.

IV. TWO CAVITY FIELDS SETUP AND PROBES OF MOMENTUM STATES

In the previous section, we have shown that cavity dissipation can be utilized to prepare the system in a steady state with desired entanglement properties. In the following sections, we show how, by using the auxiliary polarization mode a_y of the cavity field, one can get access to

the collective momentum state of the system in a non-destructive fashion.

Inspired by the experimental demonstrations in Refs. [11, 12] we consider a driving scheme that enables effective coupling of ground and excited atomic momentum states. We consider a cavity-assisted Bragg process involving the transverse driving field with amplitude η_s and frequency $\bar{\omega}$ and the cavity mode a_y with detuning ω_y , decay rate κ , and linear polarization along y [see Fig. 5(a,b)]. This process is reflected in the atom-cavity interaction term, $\propto \eta_s(a_y + a_y^\dagger) \cos kx \cos kz$ (cf. Appendix A). In this two-photon process, atoms initialized in the ground momentum state $|0\rangle_m$ can be excited to the momentum state $|1\rangle_m$, while the internal spin state ($|\downarrow\rangle_s$ or $|\uparrow\rangle_s$) remains unchanged [cf. Fig. 5(c)]. The schematics of this process are encoded in the Dicke Hamiltonian (see Appendix A)

$$H_s = \omega_y a_y^\dagger a_y + \omega_0 (J_{01}^z + J_{23}^z) + 2\eta_s (a_y + a_y^\dagger) (J_{01}^x + J_{23}^x). \quad (7)$$

Depending on the coupling η_s , the system undergoes a phase transition associated with the spontaneous breaking of the \mathbb{Z}_2 symmetry of the Hamiltonian H_s , such that the Hamiltonian is invariant under the transformation $(a_y, J^x) \leftrightarrow (-a_y, -J^x)$. When the coupling is below the critical value $\eta_s < \eta_s^c = [(\omega_y^2 + \kappa^2) \omega_0^2 / (4\omega_y)]^{1/2}$, the system is in the normal phase where only ground momentum states are occupied, and, respectively, $\langle J_{01}^z \rangle + \langle J_{23}^z \rangle = -1/2$, $\langle J_{01}^x \rangle = \langle J_{23}^x \rangle = 0$, and the cavity is empty, $n_y = \langle a_y^\dagger a_y \rangle = |\langle a_y \rangle|^2 = 0$ (see Appendix D for more details). In this phase, the condensate is homogeneously distributed within the trap without a checkerboard-like density modulation. When $\eta_s > \eta_s^c$, the system enters a \mathbb{Z}_2 symmetry-broken superradiant phase with $\langle J^x \rangle \neq 0$ and $n_y \neq 0$.

On a microscopic level, in the SR phase, the standing-wave driving field and the cavity field form an interference lattice potential $V \propto \cos kx \cos kz$, and the condensate density is modulated, forming the checkerboard lattice with the period $\lambda = 2\pi/k$, see Fig. 5(d). The density modulation originates from the condensate wave function in each spinor component. At the same time, as it is shown in Fig. 5(e), the internal spin $\Psi^\dagger \sigma \Psi$ also precesses according to the model (7) with the amplitude $\propto \sqrt{\mu(1-\mu)}$ and frequency $\propto 2\omega_s$ (see Appendix D).

The interaction term in Eq. (7) couples different atomic momentum states within the same spin manifold and does not generate entanglement between spin and momentum. Precisely, in the SR phase, the momentum configuration reads exactly the same for each spin manifold $|\uparrow\rangle_s$ and $|\downarrow\rangle_s$, and the state is separable. However, as we show below, competition between H and H_s results in a rich manifold of dynamical responses, which can be probed in a non-destructive way by analyzing the light that leaks out of the cavity [67]. As we report further in the text, by tuning η and η_s , it is possible to monitor the spin-momentum entanglement generated by η in a non-invasive manner. This means that such monitoring can

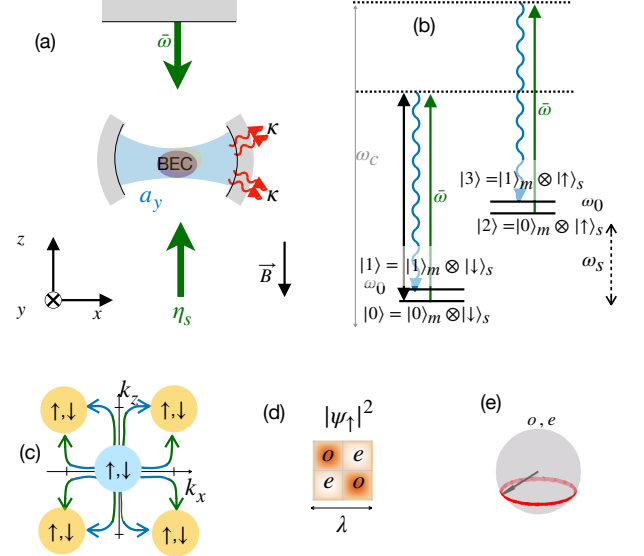


FIG. 5. (a) Schematics of the experimental setup and (b) corresponding level scheme for the model (7). (c) Momentum space cartoon for the spin-preserving Bragg process; (d) steady-state density of the condensate in the SR phase; (e) internal spin precession described by the Hamiltonian H_s . Here, spontaneous symmetry breaking in H_s results in a density checkerboard modulation.

be achieved without substantially altering the underlying dynamics of entanglement entropy.

A. Intertwined spin and momentum dynamics

The Hamiltonian describing the interaction of the two cavity modes with different polarizations and four spin-momentum levels reads

$$H_{\text{tot}} = H + H_s - \omega_0 (J_{01}^z + J_{23}^z), \quad (8)$$

where the term H_s [Eq. (7)] describes transitions in the momentum degrees of freedom, while H [Eq. (2)] describes transitions simultaneously in momentum and spin degrees of freedom. Here, we subtract the $\omega_0 J^z$ term since it is already included in both H and H_s , see derivation in Appendix A. The overall dynamics of this open system are governed by the Lindblad master equation

$$\begin{aligned} \frac{d}{dt} \rho &= -i[H_{\text{tot}}, \rho] + \kappa \mathcal{D}(\rho), \\ \mathcal{D}(\rho) &= 2a_y \rho a_y^\dagger - \{a_y^\dagger a_y, \rho\} + 2a_z \rho a_z^\dagger - \{a_z^\dagger a_z, \rho\} \end{aligned} \quad (9)$$

where we have also included a finite lifetime $\propto 1/\kappa$ for the cavity photons.

The key feature determining dynamics in this model is that the pseudo-spins J and S are built as bilinears of bosonic operators of the same Hilbert space and, therefore, in general, do not commute with each other. One

can define the matrix

$$\Sigma_{ij} = c_i^\dagger c_j = \begin{pmatrix} \Sigma_{00} & J_{01}^- & \mathcal{T}_{02}^- & S_{03}^- \\ J_{01}^+ & \Sigma_{11} & S_{12}^- & \mathcal{T}_{13}^- \\ \mathcal{T}_{02}^+ & S_{12}^+ & \Sigma_{22} & J_{23}^- \\ S_{03}^+ & \mathcal{T}_{13}^+ & J_{23}^+ & \Sigma_{33} \end{pmatrix} \quad (10)$$

which contains all the possible spin raising and lowering operators coupling the four levels of our scheme. In Σ_{ij} the diagonal elements account for the occupation of the different atomic levels; the pseudo-spins J describe transitions between different momentum states within the same spin state; the pseudo-spins S describe transitions between different momentum states within neighboring spin levels, and finally, the pseudo-spins \mathcal{T} describe transition between different spin levels but with same momentum quantum number. These operators obey a $SU(4)$ algebra with the commutation relations

$$[\Sigma_{nm}, \Sigma_{kl}] = \Sigma_{nl}\delta_{m,k} - \Sigma_{km}\delta_{n,l}. \quad (11)$$

The non-commutativity of different pseudo-spin species (and thus also $[H_s, H] \neq 0$) leads to rich dynamics [60, 61]. In particular, symmetry breaking in the subsystem governed by H can induce explicit symmetry breaking in the Hamiltonian H_s , and vice versa, see Appendix F. For instance, the superradiant phase of Hamiltonian H [Eq. (2)] corresponds to the spontaneous breaking of the \mathbb{Z}_2 symmetry of the system, such that two alternating non-zero solutions appear with $(a_z, S^x) \leftrightarrow (-a_z, -S^x)$. In terms of the underlying bosonic operators, the symmetry implies

$$\begin{aligned} c_n &\rightarrow c_n e^{-i\phi_n} \\ a_z &\rightarrow a_z e^{i\pi}. \end{aligned} \quad (12)$$

The requirement $S^x \rightarrow -S^x$ sets two constraints for four phases of the atomic fields, namely (cf. also Appendix F)

$$\begin{aligned} \phi_0 - \phi_3 &= \pi \pm 2\pi n \\ \phi_2 - \phi_1 &= \pi \pm 2\pi m. \end{aligned} \quad (13)$$

As a result, if the coupling η_s is non-vanishing, the symmetry of the interacting term in the Hamiltonian H_s will be explicitly broken by the emergent phase $\pm(\phi_1 - \phi_3)$, $2J^x \rightarrow -(J_{01}^- e^{i(\phi_3 - \phi_1)} + J_{23}^- e^{-i(\phi_3 - \phi_1)} + h.c.)$, which can not be compensated by the phase of a_y . This explicit symmetry breaking manifests in the onset of long-lived non-stationary dynamical responses, even though the Hamiltonian possesses a \mathbb{Z}_2 symmetry, and thus, it would be in general expected to relax into a time-independent steady state [68]. On the contrary, in the normal state, the emergent phase $\phi_1 - \phi_3$ can be immediately set to $2\pi n$ (both excited momentum states are unpopulated and $\langle c_1 \rangle = \langle c_3 \rangle = 0$) and the spontaneous symmetry breaking does not bring any observable effect to the dynamics. Finally, spontaneous symmetry breaking in H_s induces explicit symmetry breaking in H . For a detailed discussion, refer to Appendix F.

We want to emphasize that considering a four-level model is essential for obtaining the above-mentioned non-stationary phases. For instance, omitting the atomic level $|0\rangle$ in H_{tot} to get an effective three-level description relaxes the constraints of Eq. (13) and prevents dynamics arising from explicit symmetry breaking (see Appendix H for a comprehensive discussion).

V. PROBING DYNAMICS WITH THE TWO CAVITY FIELDS

We now discuss the different dynamical regimes arising from the interplay of H_s and H . We show how the auxiliary cavity field dynamics are directly linked with spin precession and entanglement entropy oscillations, facilitating continuous monitoring of the system's dynamics.

A. Dynamical phase diagram

By tuning the two couplings, η (spin-momentum) and η_s (momentum) below and above criticality, we generate the complete diagram of dynamical responses, reported in Fig. 6(a). We initialize the system in the normal state [69] and then fast ramp it at certain values of the couplings [cf. Appendix C].

As order parameters, we consider the mean field expectation values of two cavity fields, $\langle a_y \rangle$ and $\langle a_z \rangle$. The choice is convenient for two reasons. Firstly, typical experiments operate in a regime where cavity detunings, $\omega_{y,z}$, and decay rates, κ , are a few orders of magnitude larger than atomic energy scales [10–12, 36]. Consequently, one can adiabatically eliminate the cavity modes since on timescales $\propto 1/\kappa$ they approach the steady state values $\langle a_y \rangle \approx -2\eta_s(\langle J_{01}^x \rangle + \langle J_{23}^x \rangle)/(\omega_y - i\kappa)$, $\langle a_z \rangle \approx -2\eta(\langle S_{03}^x \rangle + \langle S_{12}^x \rangle)/(\omega_z - i\kappa)$ [70]. Thus, the cavity fields $\langle a_y \rangle$ and $\langle a_z \rangle$ offer direct information about momentum $\langle J^x \rangle$ and spin-momentum $\langle S^x \rangle$ coherences in the system. Notice that the naïve elimination of the cavity field at the level of the generator of dynamics would result in a lack of relaxation, which is an artifact (in the Dicke model, the decay appears at the higher order of perturbation theory; see Refs.[36, 71, 72] for a comprehensive discussion). Indeed, in order to extract the dynamical responses in Fig. 6, we adopt a Redfield master equation approach [70, 71]; the corresponding equations of motion are reported in Appendices B, C.

The second reason to use cavity fields as order parameters is their experimental accessibility. Using heterodyne detection [67], which gives access to the magnitude and phase of the cavity fields, it is possible to conduct continuous non-destructive measurements of the system. In contrast, imaging the condensate's spin and density distribution constitutes a destructive measurement, requiring numerous experiment repetitions to reconstruct dynamics.

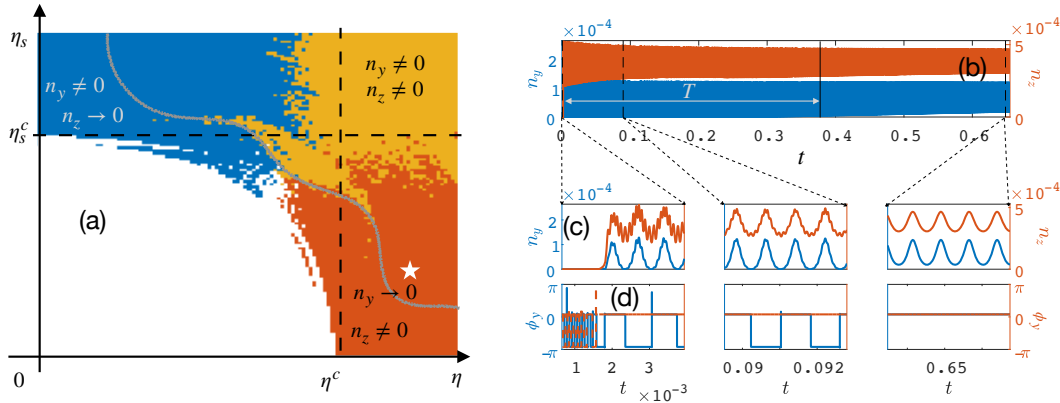


FIG. 6. (a) Dynamical phase diagram with three possible self-organized phases in blue, yellow, and orange. Different phases are distinguished from the dynamics of the two cavity fields $\langle a_y \rangle$ and $\langle a_z \rangle$. Gray line separates parameters for which the explicitly broken symmetry restores during finite (above the line) or infinite (below the line) time. (b) Time evolution of the occupation number for the two cavity modes, for parameters marked with a star in panel (a). (c) Zoom on the dynamics of the photon number and (d) phase at the beginning, middle, and end of time evolution in panel (b). Time is given in seconds, see main text. Here we fix $\omega_y = \omega_z = 5\kappa$, $\omega_s = \omega_0/4$, $\mu = 0.75$.

The system exhibits a variety of self-organization transitions, distinguishable by the dynamics of the cavity fields $\langle a_y \rangle$ and $\langle a_z \rangle$. Firstly, when both couplings are smaller than the critical ones [white region in Fig. 6(a)], the system remains in the normal state with zero occupation of the cavity fields. In terms of atomic degrees of freedom, the internal atomic pseudo-spin precesses with the frequency $2\omega_s$ and amplitude given by $\sqrt{1/4 - \langle \mathcal{T}^z \rangle^2} = \sqrt{\mu(1 - \mu)}$.

By increasing η above the critical value and keeping $\eta_s < \eta_s^c$, the system undergoes a phase transition to the SR phase, associated with breaking of the \mathbb{Z}_2 symmetry of H [cf. Eq. (2)]. The occupation of the cavity mode $\langle a_z \rangle$, together with the pseudo-spin $\langle S^x \rangle$ become non-zero [see red region in Fig. 6(a)]. On the other hand, according to the transformation (12), this spontaneous symmetry breaking also induces explicit symmetry breaking in H_s [Eq. (7)], namely, the interaction term gains a phase $\pm(\phi_1 - \phi_3)$. As a consequence, the pseudo-spin $\langle J^x \rangle$ starts precessing with a zero time average, resulting in periodic development of $\langle a_y \rangle \propto \langle J^x \rangle$. In this way, subsystem (7) experiences superradiance from the interaction with the subsystem (2); otherwise, since $\eta_s < \eta_s^c$, the pseudo-spin $\langle J^x \rangle$ together with the cavity field $\langle a_y \rangle$ remain in the normal state.

In the experiment, this dynamical phase can be discerned by measuring both the photon number and phase of the two cavity fields, as illustrated in Fig. 6(b-d). Following the fast ramp at $t = 0$, the observable $n_z = \langle a_z^\dagger a_z \rangle$ approaches a non-zero value. Simultaneously, the photon number of the second mode, denoted as $n_y = \langle a_y^\dagger a_y \rangle$, undergoes oscillations, transitioning from zero to a finite value. At each instance when n_y returns to zero, the phase $\phi_y = \arg(\langle a_y \rangle)$ experiences a discrete shift of π , signifying that $\langle a_y \rangle$ undergoes a sign reversal, as shown in

Fig. 6(c,d). Note that depending on parameters, such a regime with the zero-averaged $\langle a_y \rangle$ and periodic jumps of ϕ_y can take finite time, which we denote T in Fig. 6(b). This time is linked to the propensity of the system to restore explicitly broken symmetry and, as we show in the following section, the finiteness of T can be related to the possibility of non-invasive continuous monitoring of the entanglement dynamics. In Fig. 6(a) for parameters below the gray line in panel (a) $T \rightarrow \infty$, while for parameters above the line, it takes a finite value.

In the regime where the field $\langle a_y \rangle$ oscillates with zero average, the precession frequency of the pseudo-spin $\langle J^x \rangle$ can be calculated as the inverse of the time interval over which the phase of $\langle a_y \rangle$ changes by 2π . Simultaneously, the amplitude of $\langle J^x \rangle$ oscillations can be deduced from the maximum value of n_y during one period, $\text{ampl}(\langle J^x \rangle) = [\max(n_y)(\omega_y^2 + \kappa^2)]^{1/2}/(2\eta_s)$.

The time evolution shown in Fig. 6(b-d) is not unique but depends on the phase that is initially imprinted in the boson c_i (pseudo-spins Σ_{ij}) operators. Different initial conditions can lead to dephasing and variations in the amplitudes and frequencies for different observables due to the nonlinear nature of the problem. However, as we have checked numerically, the oscillatory behavior in Fig. 6(c-d) is generic for different realizations of the initial conditions, meaning one can observe oscillations of the magnitude of the cavity fields and also periodic jumps of the phase of the auxiliary cavity field.

In the opposite limit, when $\eta_s > \eta_s^c$ and η is below its critical value [blue region in Fig. 6(a)], the transition to the SR phase takes place in cavity field $\langle a_y \rangle$ and pseudo-spin $\langle J^x \rangle$, while cavity mode $\langle a_z \rangle$ experiences oscillations with zero time-average. These oscillations appear due to the explicit symmetry breaking in Hamiltonian H in Eq. (2) and subsequent precession of the pseudo-spin

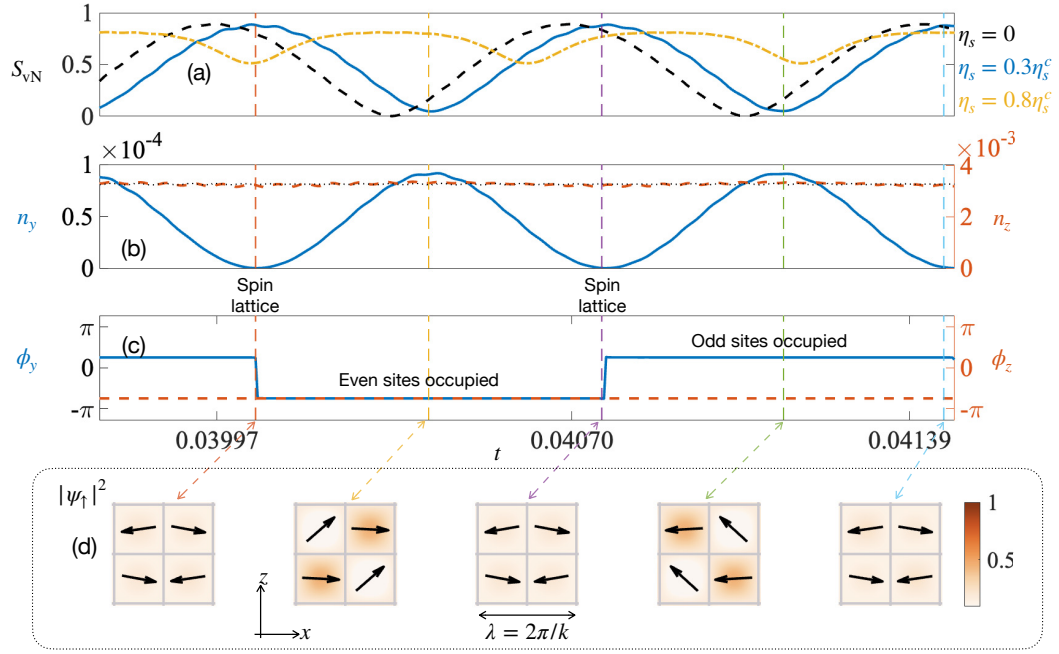


FIG. 7. (a) Dynamics of the entanglement entropy, (b) occupation of the cavity modes, (c) phases of the cavity modes, and (d) real space density in the red region in the phase diagram. The black line in panel (a) corresponds to the $\eta_s = 0$ case, while red and blue lines correspond to the dynamics with non-zero $\eta_s \ll \eta_s^c$. From oscillations of the cavity field phase ϕ_y , one can recover the structure of the real-space checkerboard lattice: when $\phi_y > 0$ odd sites are occupied, and when $\phi_y < 0$ even sites are more occupied. The $n_y = 0$ case corresponds to the maximally entangled state in which the checkerboard is formed by the projection of the spin on the x axis rather than the density lattice.

$\langle S^x \rangle$. Similarly to the previous case, the precession period is equal to the time interval during which $\phi_z = \arg(\langle a_z \rangle)$ changes by 2π , and the amplitude of $\langle S^x \rangle$ oscillations is $\text{ampl}(\langle S^x \rangle) = [\max(n_z)(\omega_z^2 + \kappa^2)]^{1/2}/(2\eta)$.

Finally, when both couplings are above the critical ones [see the yellow region in Fig. 6(a)], both cavity modes, $\langle a_y \rangle$ and $\langle a_z \rangle$, become non-zero, and the symmetry of both H_s in Eq. (7) and H in Eq. (2) are spontaneously broken in a self-consistent way. Here, both cavity fields have fixed phases, while their magnitudes can oscillate while the system approaches a (stationary) steady state.

B. Slow relaxation in multi-level Dicke model

The oscillations shown in Fig. 6(b) persist far longer than the operational timescales of the experiment. Below, we discuss the mechanism that induces such prolonged relaxation in the dissipative model (8).

The evolution of energy in the two-level Dicke model during relaxation is given by $d\langle E \rangle/dt = \kappa \mathcal{D}(\omega_c a^\dagger a + 2\eta(a + a^\dagger)J^x)$, which in terms of spin degrees of freedom is proportional to $d\langle E \rangle/dt \propto \langle J^x \rangle \langle J^y \rangle$. In the steady state $\langle J^y \rangle = 0$ and the system's energy is constant, indicating that all energy pumped from the external driving fields is completely lost through the dissipation of the cavity mode. However, on its way to stationarity, the spin component $\langle J^y \rangle$ oscillates around zero value, which means

that with period $2\omega_0$ energy is pumped in (negative $\langle J^y \rangle$) and out (positive $\langle J^y \rangle$) of the system, leading to the relaxation time $\tau = (\omega_y^2 + \kappa^2)/(\omega_0^2 \kappa) \gg 1/\kappa$ [68, 72].

In contrast, in the four-level model (8), the superradiance in one spin species acts as an ‘effective drive’ for the other, inducing an additional factor that slows down the relaxation. Here, the explicit breaking of the Hamiltonian symmetry results in the generation of non-stationary phases. It happens due to the competing conditions on the phases of the boson fields, ϕ_0, \dots, ϕ_3 , set by H [Eq. (2)] and H_s [Eq. (7)]. Relaxation in the four-level model (8) is conditioned from the temporal evolution of phases of the boson operators $\phi_{1,\dots,3}$, whose interdependence slows down reaching a steady state, as it happens in constrained models [73, 74]. Such slow relaxation is crucial for the continuous read-out of the system's dynamics since spin precession can be easily captured at extensive timescales.

C. Read-out

We now relate the dynamics of the auxiliary cavity field $\langle a_y \rangle$ to the evolution of both the entanglement entropy S_{vN} and the condensate's microscopic degrees of freedom. An instance of such dynamics for parameters as in the red region in Fig. 6 ($\eta_s = 0.3\eta_s^c$, $\eta = 1.6\eta^c$) is shown in Fig. 7. Here, the blue line in panel (a) shows the

dynamics of the entanglement entropy, panel (b) the dynamics of the populations of the two cavity modes, panel (c) the dynamics of the phase of two cavity fields, and finally panel (d) shows snapshots of the condensate density at different times. Arrows in panel (d) indicate spin magnetization in the centers of the checkerboard lattice sites.

The oscillations of the photon number $n_y = \langle a_y^\dagger a_y \rangle$ [panel(b)] and the phase $\phi_y = \arg(\langle a_y \rangle)$ [panel (c)] capture precession of the external pseudo-spin $\langle J^x \rangle$, as $\langle a_y \rangle \approx -2\eta_s(\langle J_{01}^x \rangle + \langle J_{23}^x \rangle)/(\omega_y - i\kappa)$. When the phase of the cavity field changes by $\pm\pi$, the real space density checkerboard lattice changes its parity [odd or even lattice sites are more occupied, see panel (d)]. Concomitantly, the system reaches the maximum value of the entanglement entropy [panel (a)]. At the same time, the checkerboard lattice with period $\lambda = 2\pi/k$ is formed not by modulation of the density but rather by the different orientations of the spin in the centers of even and odd sites.

When the phase of the field $\langle a_y \rangle$ gains $\pm\pi$ jump, the spatial density profile changes parity. At the same time, the increase of the photon number n_y indicates a decrease of entanglement since the coupling η_s tends to disentangle spin and momentum, while a decrease of n_y , on the other hand, indicates the developing of the spin-momentum correlations in the system. In this way, one can capture real-time oscillations of the entanglement entropy from the oscillations of the cavity field $\langle a_y \rangle$.

Finally, the fixed phase of the cavity field a_z , $\phi_z = \arg(\langle a_z \rangle)$, indicates the spontaneous symmetry breaking in H [cf. Eq. (2)]. In terms of the atomic degrees of freedom, the fixed phase ϕ_z in panel (c) captures the absence of the mirror symmetry between maximally entangled states, namely for two consecutive maximally entangled states, the spin lattices are exactly the same, without the symmetry under swapping even and odd sites, cf. even panels in Fig. 7(d).

The heterodyne detection of two cavity modes a_y and a_z enables distinguishing different dynamical phases in the system in a non-destructive way. However, by itself, the coupling to the auxiliary cavity mode can change the steady state properties and, more importantly in the context of this paper, change the entanglement of the system compared to the single-mode model. In this regard, it is important to separate a range of couplings for which utilizing additional polarization preserves most of the entanglement and, at the same time, is sufficient to perform measurements. We dedicate the next Section to this aim.

VI. ENTANGLEMENT IN THE TWO PHOTON FIELDS MODEL

In this Section, we revisit the system's various dynamical responses in terms of spin-momentum entanglement generation when both cavity modes contribute to the dy-

namics and identify parameter ranges suitable for non-invasive monitoring of the dynamics of collective observables. We show criteria to determine the range of parameters for which the auxiliary cavity mode creates a minimal backaction on the system's dynamics. For all extra details, we refer the reader to Appendix G.

The entanglement properties of the system are conditioned from the competition between η [which couples spin-momentum pseudo-spins with cavity mode a_z and tries to entangle spin and momentum] and η_s [which couples momentum pseudo-spins J with the cavity field a_y and tends to maintain spin and momentum separable]. Fig. 8 shows numerical data on the maximal entanglement $\max(S_{vN})$ as a function of these 'spin-momentum' η and 'momentum' η_s couplings. Here, we maintain the same parameters as those in the phase diagram of Fig. 6(a). The plot shows that increasing η induces stronger correlations between spin and momentum, while η_s acts as a disentangling agent.

The interplay between η and η_s can significantly alter not only the $\max(S_{vN})$ but also the steady-state properties of the system along with the evolution of the S_{vN} compared to the $\eta_s = 0$ case. Fig. 7(a) shows the evolution of the S_{vN} for weak, strong, and zero coupling η_s to the auxiliary mode a_y . Compared to the unprobed model ($\eta_s = 0$, black line), for weak values the photon-matter coupling slightly modifies the steady state and entanglement dynamics ($\eta_s = 0.3\eta_s^c \ll \eta_s^c$, blue line), while for strong values, it can alter dynamics of the S_{vN} significantly ($\eta_s = 0.8\eta_s^c$, yellow line). These regimes can be distinguished from the dynamics of the auxiliary field. For weak couplings, the read-out is non-invasive, and the auxiliary field oscillates with the zero time average for timescales that significantly exceed the operational timescale of the experiment ($t_{op} \propto 0.01$ s). In the experiment, these oscillations correspond to periodic changes in the phase of the auxiliary field. In the strong coupling regime, the read-out procedure is invasive, and the phase of the auxiliary field becomes fixed after some time, T , which is comparable with the operational timescale of the experiment. At this time, the explicitly broken symmetry of the Hamiltonian is restored, and the system starts evolving toward the SR state for both cavity fields.

The restoration of the symmetry indicates the change in the steady state and, thus also entanglement properties of the system. Because of this, for non-destructive probing of the dynamics, it would be convenient to work in a parameter regime where $T/t_{op} \rightarrow \infty$. Our numerics suggests that $T \propto \exp(\eta_s - \eta_s^c)$, revealing that symmetry restoration occurs more rapidly as the coupling to the auxiliary mode approaches the critical threshold, cf. Appendix G. As such, for non-destructive monitoring dynamics, it is essential to maintain the coupling to the auxiliary field significantly below the critical value.

Combining the information on relaxation timescales with the amount of entanglement generated in Fig. 8 (see Appendix C for more details), it appears that in the limit of $\eta \gg \eta^c$ and $\eta_s \ll \eta_s^c$ (parameters region, separated by

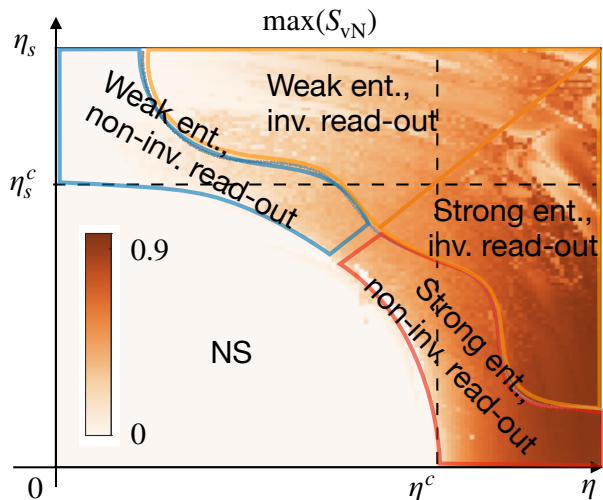


FIG. 8. Maximum value of the entanglement entropy at late times as a function of the couplings η and η_s . Parameters are the same as in Fig. 6. The cartoon in Fig. 1(c) is sketched from the data of this figure. Blue, yellow, and orange lines are added to distinguish different regimes in terms of the amount of spin-momentum entanglement and the invasiveness of the read-out procedure.

the red lines in Fig. 8) highly entangled states are prepared, while the system keeps oscillating for long times, facilitating the reconstruction of oscillations of the entanglement entropy by measuring the auxiliary cavity field $\langle a_y \rangle$ (cf. Fig. 7). On the other hand, in the part of the phase diagram dominated by the coupling η_s , there is no strong entanglement, albeit η can still induce short-lived spin-momentum correlations (see parameters region, separated by the blue line in Fig. 8). Finally, when both couplings are high enough (see parameters region separated by yellow lines), probing the system's dynamics with the auxiliary cavity field alters dynamics significantly, and T is finite.

By adjusting experimentally accessible parameters, such as couplings η , η_s and detuning ω_s , one can tune the amplitude, time-average, and oscillation frequency of the entanglement entropy, thereby dynamically controlling the correlation between spin and momentum. In principle, the simplest approach is to set $\omega_y/\kappa \rightarrow 0$, which ensures that pseudo-spins do not receive any feedback from a_y , and thus, all entanglement properties are solely determined by light-matter interactions contained in H . In this case, the dissipation induces a phase shift of the auxiliary cavity field, $\phi_\kappa^y = \tan^{-1}(-\kappa/\omega_y) = \pi/2$ [11], making it imaginary, $\langle a_y \rangle + \langle a_y^\dagger \rangle = 0$, and reducing back-action of the field a_y on the H , see Appendix G. However, the effective model with H_{tot} [Eq. (8)] breaks down for these extreme conditions because the many-body description of the model, in this case, requires taking into account higher momentum modes.

A more practical scenario is when the frequency of the auxiliary cavity photon ω_y is much higher than κ . In this

case, it is easier to maintain $\eta_s/\eta_s^c \ll 1$, but have cavity occupations n_y large enough to continuously measure the collective momentum.

Furthermore, sizable stationary entanglement can be preserved when $\omega_s = 0$. Here, the Hamiltonian gains additional symmetry under the exchange of ground and excited momentum levels of two spin sub-levels, $(|0\rangle, |1\rangle) \leftrightarrow (|2\rangle, |3\rangle)$. In this case, the induced as a result of the explicit symmetry breaking phase $\pm(\phi_1 - \phi_3)$ does not evolve in time, and the explicitly broken symmetry can not be restored, see Appendix G for comprehensive discussion. For $\omega_s = 0$ the maximal and time-averaged amount of entanglement remains similar to the one generated with one main cavity mode [see Fig. 3(a)], besides a small dressing induced by η_s .

VII. CONCLUSIONS AND OUTLOOK

In this work, we have presented an experimentally feasible cavity QED platform featuring an effective four-level atomic description and shown that it manifests two intertwined self-organization transitions. This system serves as a minimal model wherein spontaneous symmetry breaking occurs in an all-to-all interacting spin model, concomitant with the formation of tunable spin-momentum entanglement. The controlled leakage of intra-cavity photons plays an important stabilization role, as the resulting dissipative dynamics facilitate convergence towards the target entangled state in a manner resilient to imperfections in the system's couplings or initial state preparation. Extending the coupling scheme with an auxiliary cavity mode gives rise to persistent oscillations (due to explicit symmetry breaking) and facilitates real-time monitoring of the system dynamics, in particular, as a proxy for entanglement.

The tunable parameters of our model facilitate a straightforward extension to spin-exchange interactions, akin to the Tavis-Cummings model [30, 36, 50]. An interesting avenue for exploration lies in understanding how quantum correlations between spin and momentum can be continuously tuned as one transitions between the Tavis-Cummings and Dicke limits considered here.

We should note that a relation between multi-level atoms and entanglement has been previously reported both in cavity QED systems [29, 75–77] and photonic waveguides [9, 78–81]. In these cases, entangled states can be hosted within the sub-radiant subspaces of the multi-level atoms, with level degeneracies being crucial for the build-up of quantum correlations. The mechanism is markedly different from ours, although considering a combination of the two setups could naturally lead to further interesting developments.

Taking a broader perspective, one could investigate how different dynamical phases of matter routinely engineered in cavity QED would morph, when both spin and momentum degrees of freedom are optically addressed.

Our analysis has focused on the superradiant phase transition as a paradigmatic case, but it would be intriguing to see whether entanglement properties of spin-momentum hybridized states can be manipulated as a response to periodic drives [16, 17, 82] or in the context of dissipative-induced phase transitions [11, 15, 18, 30, 83].

ACKNOWLEDGMENTS

The authors thank Tilman Esslinger for fruitful discussions. O. C. is grateful to M. Stefanini and R.J. Valencia-Tortora for many useful discussions. This project has been supported by the Deutsche Forschungsgemeinschaft (DFG, German Research Foundation) – Project-ID 429529648 – TRR 306 QuCoLiMa “Quantum Cooperativity of Light and Matter”) and by the QuantERA II Programme that has received funding

from the European Union’s Horizon 2020 Research and Innovation Programme under Grant Agreement No 101017733 (‘QuSiED’) and by the DFG (project number 499037529). We acknowledge funding from the Swiss National Science Foundation (project No. 212168 and IZBRZ2.186312), from EU Horizon 2020 (European Research Council advanced grant TransQ, project no. 742579) and from the Swiss Secretariat for Education, Research and Innovation (SERI). J.M. and O.C. acknowledge support from the Dynamics and Topology Centre funded by the State of Rhineland Palatinate. K.S. acknowledges funding from NSF EAGER-QAC-QCH award No. 2037687. The authors gratefully acknowledge the computing time granted on the supercomputer MOGON 2 at Johannes Gutenberg-University Mainz (hpc.uni-mainz.de).

Appendix A: Derivation of the Hamiltonian

In this Appendix, we present a derivation of Hamiltonian H_{tot} for a setup depicted in Figs. 2 and 5. The derivation of the Hamiltonian H or H_s can be obtained by setting $E_s = 0$ or $E_b = E_r = 0$ below respectively.

We start with the general Hamiltonian for the light-matter interaction problems, which reads

$$H_{\text{tot}} = H_c + H_a + H_{\text{int}}, \quad (\text{A1})$$

where H_c governs dynamics of the cavity mode, H_a is single-atom Hamiltonian and H_{int} describes interaction between atom and the cavity. We specify the explicit form of H_c , H_a and H_{int} in the considered setup and show under which assumptions the low-energy physics of the model can be simulated by Eq. (8).

We immerse ^{87}Rb atoms inside an optical cavity oriented along the \mathbf{e}_x axis. The cavity has a single relevant frequency $\omega_c = 2\pi \cdot 382.04685$ THz with a decay rate of $\kappa \sim 2\pi \cdot 1.25$ MHz, and two polarizations \mathbf{e}_y and \mathbf{e}_z in the transverse plane. We represent two corresponding cavity polarization modes by operators a_y and a_z , respectively. The cavity Hamiltonian reads

$$H_c = \hbar\omega_y a_y^\dagger a_y + \hbar\omega_z a_z^\dagger a_z. \quad (\text{A2})$$

We apply a classical pump field with the standing-wave profile along \mathbf{e}_z (perpendicular to the cavity axis) and a Gaussian profile in the transverse directions, along \mathbf{e}_x and \mathbf{e}_y . We consider a dispersive regime, in which pumping frequency is chosen out-of-resonance with the electron transition $5^2S_{1/2} \rightarrow 5^2P_{1/2}$, $5^2P_{3/2}$. In this case, excited atomic states can be eliminated, and the resulting atomic Hamiltonian within the $F = 1$ hyperfine manifold of the $5^2s_{1/2}$ level reads

$$H_a = \frac{\mathbf{p}^2}{2M} + V_{\text{ext}} + \sum_{F, m_F} \hbar\omega_{F, m_F} |F, m_F\rangle \langle F, m_F|, \quad (\text{A3})$$

where \mathbf{p} is the momentum of the atom, M is the atomic mass, V_{ext} describes an external trapping potential, and the energy of atomic level $|F, m_F\rangle$ is $\hbar\omega_{F, m_F}$. The sum in the last terms runs over all atomic levels in $F = 1$ manifold. We apply a strong magnetic field $\mathbf{B} = -B\mathbf{e}_z$ along z direction, which induces first and second-order Zeeman splitting between levels with different magnetic numbers m_F . Introducing internal spin operator $\mathbf{F} = (F^x, F^y, F^z)$, the atomic part of the Hamiltonian can be rewritten

$$H_a = \frac{\mathbf{p}^2}{2M} + V_{\text{ext}} + \hbar\omega_z^{(1)} F^z + \hbar\omega_z^{(2)} (F^z)^2, \quad (\text{A4})$$

where $\omega_z^{(1)} < 0$ and $\omega_z^{(2)} > 0$ are the first and the second order Zeeman splittings.

The atoms are neutral and are much smaller than the wavelength of the optical light fields so that the light-matter interaction can be described in the dipole approximation

$$H_{\text{int}} = -\mathbf{d}_{\text{lab}}\mathbf{E}_{\text{lab}}, \quad (\text{A5})$$

where the atomic dipole operator can be expanded in terms of the atom's internal states

$$\mathbf{d}_{\text{lab}} = \sum_{e,g} \mathbf{d}_{eg} |e\rangle \langle g| + \text{h.c.}, \quad \mathbf{d}_{eg} = \langle e|\mathbf{d}|g\rangle. \quad (\text{A6})$$

The total optical field \mathbf{E}_{lab} is the sum of the classical pump field, $\mathbf{E}_p(\mathbf{r})$, and the cavity field, $\mathbf{E}_c(\mathbf{r})$. The classical pump field with the polarization along \mathbf{e}_y , has a standing-wave profile in the longitudinal direction (\mathbf{e}_z) and a Gaussian profile in the transverse direction (along $\mathbf{e}_x, \mathbf{e}_y$):

$$\mathbf{E}_p(\mathbf{r}) = \mathbf{e}_y \sum_{\beta=b,r,s} \frac{E_\beta}{2} f_\beta(\mathbf{r}) e^{-i\omega_\beta t} + \text{h.c.}, \quad (\text{A7})$$

with the mode function for each sideband is $f_\beta(\mathbf{r}) \equiv f(\mathbf{r}) = \exp(- (2x^2/w_x^2 - 2y^2/w_y^2)) \cos(k_\beta z)$. The widths of the transverse Gaussian profile are approximately $w_x, w_y \approx 25 \mu\text{m}$. The wave-vectors are $k_\beta = \omega_\beta/c \approx \omega_p/c$ with c denoting speed of light. To induce the atomic transitions, discussed in Sec. II and Sec. IV, we consider three laser drivers $\beta = b, r, s$, with the sideband frequencies $\omega_{b(r)}$ such that detunings $\delta\omega_\beta = \omega_\beta - \omega_p$ are chosen to correspond to the differences in first-order Zeeman shifts (in the $F = 1$ ground state manifold). In contrast, the third detuning is set to be zero, $\omega_s = (\omega_b + \omega_r)/2 = \bar{\omega}$. In this case, different driving schemes operate with the same momentum states. We limit our consideration to the case when $E_b = E_r \neq E_s$.

The cavity field TEM00 mode of a Fabry-Perot cavity has a standing-wave profile in the transverse direction (\mathbf{e}_x) and a Gaussian profile in the other two directions along \mathbf{e}_y and \mathbf{e}_z :

$$\mathbf{E}_c(\mathbf{r}) = \mathbf{e}_y E_c g_y(\mathbf{r}) a_y + \mathbf{e}_z E_c g_z(\mathbf{r}) a_z + \text{h.c.} \quad (\text{A8})$$

where the mode functions are $g_{y,z}(\mathbf{r}) \equiv g(\mathbf{r}) = \exp(- (2(y^2 + z^2))/w_c^2) \cos(k_c x)$ with the Gaussian profile having a width of approximately $w_c \approx 25 \mu\text{m}$. The wave-vectors are $k_{y,z} \approx k_c = \omega_c/c$.

As we are working in the dispersive regime, the excited atomic states can be eliminated using the Schrieffer-Wolff [84] transformation $H \rightarrow e^S H e^{-S}$, $[S, H_0] = -H_{\text{int}}$, which results in the low-energy Hamiltonian

$$\begin{aligned} H_0 &= \frac{\mathbf{p}^2}{2M} + V_{\text{ext}} + \hbar\omega^{(1)} F^z + \hbar\omega^{(2)} (F^z)^2 + \hbar\omega_c^y a_y^\dagger a_y + \hbar\omega_c^z a_z^\dagger a_z \\ H_{\text{int}}^s &= \alpha_s f^2(\mathbf{r}) \left| \sum_{\beta} \frac{E_\beta}{2} e^{i\delta\omega_\beta t} \right|^2 + \alpha_s |E_c|^2 g^2(\mathbf{r}) (a_y^\dagger a_y + a_z^\dagger a_z) \\ &+ \alpha_s \overbrace{(\mathbf{e}_y \cdot \mathbf{e}_y)}^{=1} f(\mathbf{r}) g(\mathbf{r}) \sum_{\beta} \frac{E_\beta}{2} (e^{i\omega_\beta t} a_y + e^{-i\omega_\beta t} a_y^\dagger) + \alpha_s \overbrace{(\mathbf{e}_y \cdot \mathbf{e}_z)}^{=0} f(\mathbf{r}) g(\mathbf{r}) \sum_{\beta} \frac{E_\beta}{2} (e^{i\omega_\beta t} a_z + e^{-i\omega_\beta t} a_z^\dagger) \\ H_{\text{int}}^v &= -i \frac{\alpha_v}{2F} g(\mathbf{r}) f(\mathbf{r}) \sum_{\beta} \frac{E_c E_\beta}{2} \left[(a_y e^{i\omega_\beta t} - a_y^\dagger e^{-i\omega_\beta t}) \overbrace{(\mathbf{e}_y \times \mathbf{e}_y)}^{=0} \cdot \mathbf{F} + (a_z e^{i\omega_\beta t} - a_z^\dagger e^{-i\omega_\beta t}) \overbrace{(\mathbf{e}_y \times \mathbf{e}_z)}^{=e_x} \cdot \mathbf{F} \right] \\ &- \underbrace{i \frac{\alpha_v}{2F} E_c^2 g^2(\mathbf{r}) (a_y^\dagger a_z - a_z^\dagger a_y) (\mathbf{e}_y \times \mathbf{e}_z) \cdot \overbrace{\mathbf{F}}^{\alpha_e \pm i\omega t}}_{=0, \text{ because of resonance conditions}} \end{aligned} \quad (\text{A9})$$

For the transitions in multi-level atoms, it is convenient to account for selection rules using polarizabilities. In the above equation, $\alpha_{s,v}$ are scalar and vector polarizabilities of the atoms, which are components of the rank-2 tensor $\alpha_{i,j} = \sum_{g,g'} \sum_e \langle g|d_i|e\rangle \langle e|d_j^\dagger|g'\rangle |g\rangle \langle g'| / (\hbar\Delta_e) = \alpha_s \text{Id}_{ij} - i\alpha_v / (2F) \epsilon_{ijk} + \dots$. Here, diagonal components, proportional to α_s , describe the process when the spin of the atom remains unchanged, while vectorial non-diagonal components, proportional to α_v , describe the transition of the spin state of the atom after the two-photon process. The sum runs over all allowed transitions (see Ref. [85]), $d_i = (\mathbf{d}\mathbf{e}_i)$ is the i -th component of the atomic dipole moment, $i = \{x, y, z\}$, and the detuning of the driving field from the resonance frequency is $\Delta_e \approx \omega_p - \omega_e$.

Finally, we move to a frame rotating with the classical pump frequency: $H_{\text{lab}} \rightarrow H = U_p^\dagger H_{\text{lab}} U_p - H_p$ where $U_p = \exp(-iH_p t/\hbar)$ and $H_p = \sum_e \hbar\omega_p |e\rangle \langle e| + \hbar\omega_p (a_y^\dagger a_y + a_z^\dagger a_z)$. The rotating-wave approximation brings us to the time-independent single-body Hamiltonian

$$H_{\text{tot}} = H_a + H_c + H_s + H_v, \quad (\text{A10})$$

$$H_a = \frac{\mathbf{p}^2}{2M} + V_{\text{ext}} + \hbar\delta^{(1)} F^z + \hbar\omega^{(2)} (F^z)^2, \quad (\text{A11})$$

$$H_c = -\Delta_y a_y^\dagger a_y - \Delta_z a_z^\dagger a_z, \quad (\text{A12})$$

$$H_s = \frac{\alpha_s}{4} f^2(\mathbf{r}) (E_s^2 + E_b^2 + E_r^2) + \alpha_s E_0^2 g^2(\mathbf{r}) (a_y^\dagger a_y + a_z^\dagger a_z) + \frac{\alpha_s}{2} f(\mathbf{r}) g(\mathbf{r}) E_0 E_s (a_y + a_y^\dagger) \quad (\text{A13})$$

$$H_v = \frac{\alpha_v}{4} E_0 E_b f(\mathbf{r}) g(\mathbf{r}) (a_z + a_z^\dagger) F^x \quad (\text{A14})$$

where $\delta^{(1)} = \omega_z^{(1)} + (\omega_b - \omega_r)/2$, $\Delta_{y,z} = \bar{\omega} - \omega_{y,z} < 0$. We have also applied a transformation $a_z \rightarrow ia_z$ to get rid of the minus sign in H_v . The first term in H_s describes the attractive potential created by the transverse driving fields, the second term describes the dispersive shift to the cavity detuning, and the last term produces the Bragg transition within the same atomic level. The vectorial interaction describes the Raman process when the transition happens between nearing sub-levels of the ground-state manifold.

Let us consider a case when the magnetic field is strong. Specifically, let the second order Zeeman shift $\omega^{(2)} \propto 1$ MHz, and thus the resonant conditions for transition $m_F = 1 \leftrightarrow m_F = 0$ are out-of-resonance for transition $m_F = 0 \leftrightarrow m_F = -1$. In this case, if we prepare the initial state as a mixture of particles at levels with $m_F = 1, 0$, the dynamics will be restricted to these two atomic levels for the typical operational times of the experiment. Thus, we can limit our consideration to the dynamics between two neighboring spin levels, defining the many-body spinor field operator

$$\Psi(\mathbf{r}) = (0, \psi_\uparrow, \psi_\downarrow)^T, \quad (\text{A15})$$

which satisfies standard bosonic commutation relations $[\psi_\sigma(\mathbf{r}), \psi_{\sigma'}^\dagger(\mathbf{r}')] = \delta_{\sigma,\sigma'} \delta(\mathbf{r} - \mathbf{r}')$, $[\psi_\sigma(\mathbf{r}), \psi_{\sigma'}(\mathbf{r}')] = 0$, where $\sigma, \sigma' = \uparrow, \downarrow$. The N -body Hamiltonian reads

$$\begin{aligned} H_{\text{tot}} &= H_c + \int d\mathbf{r} \Psi^\dagger(\mathbf{r}) (H_a + H_s + H_v) \Psi(\mathbf{r}) = \\ &= H_c + \int d\mathbf{r} \left[\frac{\alpha_s}{4} (E_s^2 + E_b^2 + E_r^2) f^2(\mathbf{r}) + \alpha_s E_0^2 (a_y^\dagger a_y + a_z^\dagger a_z) g^2(\mathbf{r}) \right] \left(\psi_\uparrow^\dagger(\mathbf{r}) \psi_\uparrow(\mathbf{r}) + \psi_\downarrow^\dagger(\mathbf{r}) \psi_\downarrow(\mathbf{r}) \right) \\ &+ \int d\mathbf{r} \psi_\uparrow^\dagger(\mathbf{r}) \left(-\frac{\hbar^2 \nabla^2}{2M} + V_{\text{ext}} \right) \psi_\uparrow(\mathbf{r}) + \int d\mathbf{r} \psi_\downarrow^\dagger(\mathbf{r}) \left(-\frac{\hbar^2 \nabla^2}{2M} + V_{\text{ext}} \right) \psi_\downarrow(\mathbf{r}) + \\ &+ \frac{\hbar\delta^{(1)}}{2} \int d\mathbf{r} \left(\psi_\uparrow^\dagger(\mathbf{r}) \psi_\uparrow(\mathbf{r}) - \psi_\downarrow^\dagger(\mathbf{r}) \psi_\downarrow(\mathbf{r}) \right) + \frac{\hbar\omega^{(2)}}{4} \int d\mathbf{r} \left(\psi_\uparrow^\dagger(\mathbf{r}) \psi_\uparrow(\mathbf{r}) + \psi_\downarrow^\dagger(\mathbf{r}) \psi_\downarrow(\mathbf{r}) \right) \\ &+ \frac{\alpha_s}{2} E_0 E_s (a_y + a_y^\dagger) \int d\mathbf{r} f(\mathbf{r}) g(\mathbf{r}) \left(\psi_\uparrow^\dagger(\mathbf{r}) \psi_\uparrow(\mathbf{r}) + \psi_\downarrow^\dagger(\mathbf{r}) \psi_\downarrow(\mathbf{r}) \right) + \\ &+ \frac{\alpha_v}{8} E_0 E_b (a_z + a_z^\dagger) \int d\mathbf{r} f(\mathbf{r}) g(\mathbf{r}) \left(\psi_\uparrow^\dagger(\mathbf{r}) \psi_\downarrow(\mathbf{r}) + \psi_\downarrow^\dagger(\mathbf{r}) \psi_\uparrow(\mathbf{r}) \right). \end{aligned} \quad (\text{A16})$$

To derive an extended Dicke Hamiltonian, we should further restrict the Hilbert space of the model by considering only the two lowest momentum states of the model for both spinor components. In this approximation the many-body wave function reads $\Psi(\mathbf{r}) = (0, \phi_0(\mathbf{r})c_0 + \phi_1(\mathbf{r})c_1, \phi_0c_2(\mathbf{r}) + \phi_1(\mathbf{r})c_3)^T$. Here, c_i are the annihilation operators of the corresponding atomic modes, $[c_i, c_j^\dagger] = \delta_{i,j}$, $[c_i, c_j] = 0$, and $\phi_1(\mathbf{r}) = \mathcal{N} \cos kx \cos kz \phi_0(\mathbf{r})$, where \mathcal{N} accounts for the correct normalization. In this notation, operators c_0 and c_2 correspond to the ground momentum states, while operators c_1 and c_3 correspond to the excited momentum states. After integrating over all space, the many-body Hamiltonian reads

$$\begin{aligned} H_{\text{tot}} &= -\hbar\tilde{\Delta}_y a_y^\dagger a_y + \hbar\omega_0 (c_1^\dagger c_1 + c_3^\dagger c_3) + \hbar\eta_s (a_y + a_y^\dagger) (c_0^\dagger c_1 + c_1^\dagger c_0 + c_2^\dagger c_3 + c_3^\dagger c_2) \\ &- \hbar\tilde{\Delta}_z a_z^\dagger a_z + \hbar\omega_s (c_2^\dagger c_2 + c_3^\dagger c_3) + \hbar\eta (a_z + a_z^\dagger) (c_1^\dagger c_2 + c_0^\dagger c_3 + c_2^\dagger c_1 + c_3^\dagger c_0), \end{aligned} \quad (\text{A17})$$

where the cavity detuning is dressed via the dynamic (dispersive) shift $\tilde{\Delta}_{y,z} = \Delta_{y,z} - \alpha_s E_0^2 N \mathcal{I} / \hbar$, the level splitting between ground and excited momentum states is equal $\omega_0 = 2\omega_{\text{rec}}$, $\omega_s = \delta^{(1)}$, and coupling constants read as follows: $\hbar\eta_s = \alpha_s E_0 E_s \mathcal{M} / 2$, $\hbar\eta = -\alpha_v E_0 E_b \mathcal{M} / 4\sqrt{2}$, where $\mathcal{I} = \int d\mathbf{r} g^2(\mathbf{r}) \phi_0^2(\mathbf{r})$, $\mathcal{M} = \int d\mathbf{r} f(\mathbf{r}) f(\mathbf{r}) \psi_1(\mathbf{r}) \psi_0(\mathbf{r})$. We have omitted standing-wave potential $\alpha_s (E_s^2 + E_b^2 + E_r^2) \int d\mathbf{r} f^2(\mathbf{r}) \phi_0^2(\mathbf{r}) / 4$ above as it only contributes to the higher momentum state and does not qualitatively modify the appearance of the phase transition discussed in the main text in Fig. 6.

Finally, one can introduce pseudo-spin operators according to Eq. (10), which brings the Hamiltonian to the following form:

$$H_{\text{tot}} = \omega_y a_y^\dagger a_y + \omega_0 (J_{01}^z + J_{23}^z) + \eta_s (a_y + a_y^\dagger) (J_{01}^+ + J_{23}^+ + J_{01}^- + J_{23}^-) + \omega_z a_z^\dagger a_z + \omega_s (S_{12}^z + S_{03}^z) + \eta (a_z + a_z^\dagger) (S_{12}^+ + S_{03}^+ + S_{12}^- + S_{03}^-), \quad (\text{A18})$$

where we set $\omega_{y,z} = -\tilde{\Delta}_{y,z} > 0$ and have normalized the Hamiltonian by $\hbar\omega_{\text{rec}}$ so that $\omega_0 = 2$ above. One should take into account that due to the particle conservation, one has $J_{01}^z + J_{23}^z = S_{03}^z - S_{12}^z$. Additionally, when $\eta = 0$, the term $\omega_s (S_{12}^z + S_{03}^z)$ can be omitted because the process $\eta_s (a_y + a_y^\dagger) (J_{01}^+ + J_{23}^+ + J_{01}^- + J_{23}^-)$ preserves the number of particles in the upper and lower spinor components, and thus the contribution to the energy of the system from the $\omega_s (S_{12}^z + S_{03}^z)$ remains constant during the whole course of the dynamics.

Appendix B: Equations of motion

In this Appendix, we derive mean-field equations of motion from the Hamiltonian in (A18). Note that for the remainder of the Appendices, we omit $\langle \cdot \rangle$ for expectation values of observables for simplicity.

The mean-field equations of motion can be easily derived from the Lindblad master equation (9) and read

$$\begin{aligned} \dot{a}_y &= -i(\omega_y - i\kappa)a_y - i\eta_s (c_0^\dagger c_1 + c_1^\dagger c_0 + c_2^\dagger c_3 + c_3^\dagger c_2) \\ \dot{a}_z &= -i(\omega_z - i\kappa)a_z - i\eta (c_1^\dagger c_2 + c_0^\dagger c_3 + c_2^\dagger c_1 + c_3^\dagger c_0) \\ \dot{c}_0 &= -i\eta (a_z + a_z^\dagger) c_3 - i\eta_s (a_y + a_y^\dagger) c_1 \\ \dot{c}_1 &= -i\omega_0 c_1 - i\eta (a_z + a_z^\dagger) c_2 - i\eta_s (a_y + a_y^\dagger) c_0 \\ \dot{c}_2 &= -i\omega_s c_2 - i\eta (a_z + a_z^\dagger) c_1 - i\eta_s (a_y + a_y^\dagger) c_3 \\ \dot{c}_3 &= -i(\omega_s + \omega_0) c_3 - i\eta (a_z + a_z^\dagger) c_0 - i\eta_s (a_y + a_y^\dagger) c_2 \end{aligned} \quad (\text{B1})$$

In terms of pseudo-spin degrees of freedom (10), the equations of motion take the following form

$$\begin{aligned}
\frac{dJ_{01}^-}{dt} &= -2i\omega_0 J_{01}^- + 2i\eta_s (a_y + a_y^\dagger) J_{01}^z + i\eta (a_z + a_z^\dagger) (\mathcal{T}_{13}^+ - \mathcal{T}_{02}^-) \\
\frac{dJ_{23}^-}{dt} &= -2i\omega_0 J_{23}^- + 2i\eta_s (a_y + a_y^\dagger) J_{23}^z + i\eta (a_z + a_z^\dagger) (\mathcal{T}_{13}^- - \mathcal{T}_{02}^+) \\
\frac{dJ_{01}^z}{dt} &= i\eta_s (a_y + a_y^\dagger) (J_{01}^- - J_{01}^+) + i\eta/2 (a_z + a_z^\dagger) (S_{12}^+ - S_{12}^- + S_{03}^- - S_{03}^+) \\
\frac{dJ_{23}^z}{dt} &= i\eta_s (a_y + a_y^\dagger) (J_{23}^- - J_{23}^+) + i\eta/2 (a_z + a_z^\dagger) (S_{12}^+ - S_{12}^- + S_{03}^- - S_{03}^+) \\
\frac{dS_{12}^-}{dt} &= 2i(\omega_0 - \omega_s) S_{12}^- + 2i\eta (a_z + a_z^\dagger) S_{12}^z + i\eta_s (a_y + a_y^\dagger) (\mathcal{T}_{02}^- - \mathcal{T}_{13}^-) \\
\frac{dS_{03}^-}{dt} &= -2i(\omega_0 + \omega_s) S_{03}^- + 2i\eta (a_z + a_z^\dagger) S_{03}^z + i\eta_s (a_y + a_y^\dagger) (\mathcal{T}_{13}^- - \mathcal{T}_{02}^-) \\
\frac{dS_{12}^z}{dt} &= i\eta (a_z + a_z^\dagger) (S_{12}^- - S_{12}^+) + i\eta_s/2 (a_y + a_y^\dagger) (-J_{01}^- + J_{01}^+ - J_{23}^- + J_{23}^+) \\
\frac{dS_{03}^z}{dt} &= i\eta (a_z + a_z^\dagger) (S_{03}^- - S_{03}^+) + i\eta_s/2 (a_y + a_y^\dagger) (J_{01}^- - J_{01}^+ + J_{23}^- - J_{23}^+) \\
\frac{d\mathcal{T}_{13}^-}{dt} &= -2i\omega_s \mathcal{T}_{13}^- + i\eta (a_z + a_z^\dagger) (J_{23}^- - J_{01}^+) + i\eta_s (a_y + a_y^\dagger) (S_{03}^- - S_{12}^-) \\
\frac{d\mathcal{T}_{02}^-}{dt} &= -2i\omega_s \mathcal{T}_{02}^- + i\eta (a_z + a_z^\dagger) (J_{23}^+ - J_{01}^-) + i\eta_s (a_y + a_y^\dagger) (S_{12}^- - S_{03}^-) \\
\frac{d\mathcal{T}_{13}^z}{dt} &= i\eta/2 (a_z + a_z^\dagger) (S_{03}^- - S_{03}^+ + S_{12}^- - S_{12}^+) + i\eta_s/2 (a_y + a_y^\dagger) (J_{23}^- - J_{23}^+ - J_{01}^- + J_{01}^+) \\
\frac{d\mathcal{T}_{02}^z}{dt} &= i\eta/2 (a_z + a_z^\dagger) (S_{03}^- - S_{03}^+ + S_{12}^- - S_{12}^+) + i\eta_s/2 (a_y + a_y^\dagger) (J_{23}^+ - J_{23}^- + J_{01}^- - J_{01}^+)
\end{aligned} \tag{B2}$$

Note that on the mean-field level, both (B1) and (B2) govern identical dynamics when the system is initially prepared in the coherent state. However, if the initial state contains higher-order correlations, one needs to consider higher-order corrections (i.e., cumulants expansion or similar methods) to capture dynamics accurately [61].

Finally, the equations of motion on the mean-field level can be derived without truncation over momentum states, starting from Hamiltonian (A16), $i\hbar\partial_t\Psi(\mathbf{r}, t) = H_{\text{tot}}(\mathbf{r})\Psi(\mathbf{r}, t)$, which results into the following equations of motion

$$\begin{aligned}
i\hbar\frac{d\psi_\uparrow(\mathbf{r})}{dt} &\approx \frac{\hbar\delta^{(1)}}{2}\psi_\uparrow(\mathbf{r}) - \frac{\hbar^2\nabla^2}{2M}\psi_\uparrow(\mathbf{r}) + \overbrace{\frac{\alpha_s}{2}E_0E_s(a_y + a_y^\dagger)f(\mathbf{r})g(\mathbf{r})\psi_\uparrow(\mathbf{r})}^{\tilde{\eta}_s} + \overbrace{\frac{\alpha_v}{8}E_0E_b(a_z + a_z^\dagger)f(\mathbf{r})g(\mathbf{r})\psi_\downarrow(\mathbf{r})}^{\tilde{\eta}} \\
i\hbar\frac{d\psi_\downarrow(\mathbf{r})}{dt} &\approx -\frac{\hbar\delta^{(1)}}{2}\psi_\downarrow(\mathbf{r}) - \frac{\hbar^2\nabla^2}{2M}\psi_\downarrow(\mathbf{r}) + \frac{\alpha_s}{2}E_0E_s(a_y + a_y^\dagger)f(\mathbf{r})g(\mathbf{r})\psi_\downarrow(\mathbf{r}) + \frac{\alpha_v}{8}E_0E_b(a_z + a_z^\dagger)f(\mathbf{r})g(\mathbf{r})\psi_\uparrow(\mathbf{r}) \\
i\hbar\frac{da_y}{dt} &\approx \hbar(\omega_y - i\kappa)a_y + \frac{\alpha_s}{2}E_0E_s \int d\mathbf{r}f(\mathbf{r})g(\mathbf{r}) \left(\psi_\uparrow^\dagger(\mathbf{r})\psi_\uparrow(\mathbf{r}) + \psi_\downarrow^\dagger(\mathbf{r})\psi_\downarrow(\mathbf{r}) \right) \\
i\hbar\frac{da_z}{dt} &\approx \hbar(\omega_z - i\kappa)a_z + \frac{\alpha_v}{8}E_0E_b \int d\mathbf{r}f(\mathbf{r})g(\mathbf{r}) \left(\psi_\uparrow^\dagger(\mathbf{r})\psi_\downarrow(\mathbf{r}) + \psi_\downarrow^\dagger(\mathbf{r})\psi_\uparrow(\mathbf{r}) \right)
\end{aligned} \tag{B3}$$

To retrieve dynamics at short times one can sufficiently simplify equations by eliminating cavity fields, substituting $a_y \approx -\alpha_s E_0 E_s \int d\mathbf{r}f(\mathbf{r})g(\mathbf{r}) \left(\psi_\uparrow^\dagger(\mathbf{r})\psi_\uparrow(\mathbf{r}) + \psi_\downarrow^\dagger(\mathbf{r})\psi_\downarrow(\mathbf{r}) \right) / (2\hbar(\omega_y - i\kappa))$ and $a_z \approx -\alpha_v E_0 E_b \int d\mathbf{r}f(\mathbf{r})g(\mathbf{r}) \left(\psi_\uparrow^\dagger(\mathbf{r})\psi_\downarrow(\mathbf{r}) + \psi_\downarrow^\dagger(\mathbf{r})\psi_\uparrow(\mathbf{r}) \right) / (8\hbar(\omega_z - i\kappa))$. Choosing periodic boundary conditions for field $\Psi(\mathbf{r})$, the resultant equations of motion can be further efficiently evaluated with the split-step Fourier transform method [86].

Both equations (B1) and (B3) describe the similar dynamical behavior of the system and transition from the normal to superradiant phase with the subsequent population of the momentum states $|1\rangle_m$ (note, that Eq. (B3) also captures population of the momentum states $|\pm 2k, 0, 0\rangle$ and $|0, 0, \pm 2k\rangle$, however for the most of the parameters the fraction of atoms there can be neglected). However, to study long-time dynamics, evaluation of (B1) can be done much more efficiently, with much less computational cost. The further simplification via proper elimination of the cavity fields is described in the following Appendix.

Appendix C: Redfield equations

To evaluate dynamics at late times, we also adiabatically eliminate dissipative cavity modes a_y and a_z and study the atom-only model. This procedure is justified by the separation of scales between cavity detunings/decay rates and atomic frequencies, which differ by two to three orders of magnitude. By applying the Schrieffer-Wolff transformation, the atom and photon modes can be decoupled, resulting in the effective atom-only description of the model. Following calculations in Refs. [70, 71], we derive the following expressions for the effective fields α_y and α_z

$$\begin{aligned}\alpha_y &= \frac{\eta_s (c_1^\dagger c_0 + c_3^\dagger c_2)}{-\omega_y - \omega_0 + i\kappa} + \frac{\eta_s (c_0^\dagger c_1 + c_2^\dagger c_3)}{-\omega_y + \omega_0 + i\kappa} \\ \alpha_z &= \frac{\eta c_3^\dagger c_0}{-\omega_z - (\omega_s + \omega_0) + i\kappa} + \frac{\eta c_0^\dagger c_3}{-\omega_z + (\omega_s + \omega_0) + i\kappa} + \frac{\eta c_2^\dagger c_1}{-\omega_z + (\omega_0 - \omega_s) + i\kappa} + \frac{\eta c_1^\dagger c_2}{-\omega_z - (\omega_0 - \omega_s) + i\kappa}.\end{aligned}\tag{C1}$$

On the mean-field level, the effective equations of motion can be derived by substituting into Eqs. B1 (α_y, α_z) instead of boson fields (a_y, a_z). The atom-only model allows us to investigate long-time dynamics and numerically explore relaxation processes. However, it is important to note that this model operates correctly when both couplings are ramped up gradually. Abrupt changes in coupling can excite high-energy excitations in the model, which are not accounted for by the Redfield equation.

To evaluate the long-time dynamical response in Fig. 6(a) (and also in Fig. 8), we initialize the system in the normal state and then ramp up both coupling during ≈ 0.002 s, which is slow enough to make Redfield description of the dynamics valid and, at the same time, fast enough to excite non-stationary phases. We then compare dynamical properties of the system ($\langle a_y \rangle, \langle a_z \rangle$) after the ramp at $t \approx 0.01$ s and at late times $t \approx 0.4$ s to distinguish between phases with the explicitly broken symmetry (which suit for non-invasive dynamics monitoring) and phases with explicitly broken symmetry, which identify strong coupling regime and invasive probing of the dynamics.

Appendix D: Analytical calculation of the steady state

Both models (7) and (2) take the form of the Dicke model and thus undergo a phase transition associated with the spontaneous breaking of \mathbb{Z}_2 symmetry. The phases associated with this symmetry breaking are the normal phase, in which all spins are polarized long z direction and occupation of the cavity photon is zero, and the superradiant phase, in which spins develop a non-zero x component, with the cavity occupation taking a non-zero value. The solution for each case can be derived as a stable stationary state of Eqs. (B2). As an illustration, let us examine the case when one of the couplings is equal to zero.

1. $\eta = 0$ case

In this case, the critical coupling is equal to $\eta_s^c = \sqrt{\omega_0 (\omega_y^2 + \kappa^2) / (4\omega_y)}$ and the solution in the SR phase read $J_{01}^z = -\mu\eta_s^{c2}/(2\eta_s^2)$, $J_{23}^z = -(1-\mu)\eta_s^{c2}/(2\eta_s^2)$, $J^x = \pm\sqrt{1/4 - J^z}$, $a_y = -\eta_s/(\omega_y - i\kappa)\sqrt{1 - \eta_s^{c4}/\eta_s^4}$. Interestingly, in this case, the spins \mathcal{T} , \mathcal{S} are not stationary but instead can precess according to the equations of motion

$$\begin{aligned}\frac{dS_{12}^-}{dt} &= 2i(\omega_0 - \omega_s)S_{12}^- + i\eta_5(a_y + a_y^\dagger)(\mathcal{T}_{02}^- - \mathcal{T}_{13}^-) \\ \frac{dS_{03}^-}{dt} &= -2i(\omega_0 + \omega_s)S_{03}^- + 1i\eta_5(a_y + a_y^\dagger)(\mathcal{T}_{13}^- - \mathcal{T}_{02}^-) \\ \frac{d\mathcal{T}_{13}^-}{dt} &= -2i\omega_s\mathcal{T}_{13}^- + 1i\eta_5(a_y + a_y^\dagger)(S_{03}^- - S_{12}^-) \\ \frac{d\mathcal{T}_{02}^-}{dt} &= -2i\omega_s\mathcal{T}_{02}^- + 1i\eta_5(a_y + a_y^\dagger)(S_{12}^- - S_{03}^-)\end{aligned}\tag{D1}$$

In the normal phase, the frequency of the precession is equal to $\pm 2\omega_s$, while in the SR phase, additional dressing from the interaction with the cavity mode a_y takes place

$$\Omega = -2\omega_s \pm \frac{4\sqrt{\omega_0^2 (\omega_y^2 + \kappa^2)^2 / 4 - \omega_y^2 (\eta_s^{c4} - \eta_s^4)}}{(\omega_y^2 + \kappa^2)}.\tag{D2}$$

These dynamics stem from the fact that three species of the pseudo-spins in the model governed by H_{tot} in Eq. (8) are built from the same boson operators, and thus, they do not commute. Consequently, spontaneous symmetry breaking in one species of the pseudo-spins can induce explicit symmetry breaking for the rest of the spin species, which results in the oscillatory behavior unless the explicitly broken symmetry is restored, see Appendix F for more details.

One can also restore the occupation of the four levels in the steady-state superradiant phase

$$\begin{aligned} c_0^\dagger c_0 &= \frac{\mu(1-2J^z)}{2} \\ c_1^\dagger c_1 &= \frac{\mu(1+2J^z)}{2} \\ c_2^\dagger c_2 &= \frac{(1-\mu)(1-2J^z)}{2} \\ c_3^\dagger c_3 &= \frac{(1-\mu)(1+2J^z)}{2}, \end{aligned} \tag{D3}$$

where μ is the fraction of atoms, initialized in state $|0\rangle$, $N_0 = Nc_0^\dagger c_0 = \mu N$.

It is worth mapping the solution in terms of spins (or bosons) back to the microscopic observables in the model (A16). In this way, one can unravel phase transition in the model (8) in the form of the self-organization transition(s) in terms of atomic degrees of freedom, such as condensate density and magnetization.

The density of the upper spinor component is $\rho_\uparrow = |\psi_\uparrow|^2 = |\langle c_0 \rangle \phi_0 + \langle c_1 \rangle \phi_1|^2 = |\langle c_0 \rangle|^2 \phi_0^2 + (\langle c_0^\dagger \rangle \langle c_1 \rangle + \langle c_1^\dagger \rangle \langle c_0 \rangle) \phi_0 \phi_1 + |\langle c_1 \rangle|^2 \phi_1^2$. The first term here is constant, while the second one takes the form $\cos kx \cos kz \propto \phi_1$ and describes the creation of the checkerboard lattice with the periodicity $2\pi/k$ when the system is in the SR phase, cf. Fig. 5(d,e). Similarly, the density of the lower spinor component reads $\rho_\downarrow = |\psi_\downarrow|^2 = |\langle c_2 \rangle \phi_0 + \langle c_3 \rangle \phi_1|^2$. At the same time, one can calculate the spatial distribution of the spin through the lattice. The three components of this spin are given by $\sigma^z = (|\psi_\uparrow|^2 - |\psi_\downarrow|^2)/2$, $\sigma_x = \text{Re}(\psi_\uparrow^* \psi_\downarrow)$, $\sigma_y = \text{Im}(\psi_\uparrow^* \psi_\downarrow)$. Here, we denote spin-1/2 operators with σ to highlight the effective two internal spin levels nature of the effective model (operator F above is defined on the spin-1 manifold). In the main text, we have plotted the values of these spins, calculated at the center of lattice cells using arrows on top of the distribution of the condensate density.

2. $\eta_s = 0$ case

The model (2) is a two-spin Dicke model with disorder in the level splittings. By deriving stationary solutions for this model, one can recover that the critical coupling, at which transition to the SR phase occurs, depends on the initial state. The resulting expression is given by Eq. (4). The S^z spin components can be further found from $\left[(\omega_s + \omega_0) + \frac{2\omega_z \eta^2}{\omega_z^2 + \kappa^2} S_z^{03} \right] S_x^{03} = 0$ and $\left[(\omega_s - \omega_0) + \frac{2\omega_z \eta^2}{\omega_z^2 + \kappa^2} S_z^{12} \right] S_x^{12} = 0$. Also, note that when one or both of the level splittings $\omega_0 \pm \omega_s$ become negative, the initial state with particles prepared in the ground momentum state $\psi = \sqrt{\mu}|0\rangle + \sqrt{1-\mu}|2\rangle$ is effectively a population inverted state. Thus, the transition to the SR phase appears on longer timescales after the system relaxes to the ground state (corresponding to an excited momentum state). In this case, one can first observe decay with a ‘burst’ of atoms to the excited momentum states $|1\rangle$ and $|3\rangle$, and then approach the correct SR state with a finite population of ground and excited momentum states.

As it is illustrated in the main text, the SR transition in the spin S , which is built simultaneously from different momentum and spin atomic states [cf. Eq. (1)], can act as driving for both spin and density (momentum) of the BEC. Examples of such non-stationary behavior of internal/external degrees of freedom are shown in Fig. 2(d,e) and Fig. 4(b-c). This non-stationary behavior also can be seen by analyzing equations of motion for pseudo-spins \mathcal{T} and J :

$$\begin{aligned} \frac{dJ_{01}^-}{dt} &= -2i\omega_0 J_{01}^- + 2i\eta \text{Re}(a_z)(\mathcal{T}_{13}^+ - \mathcal{T}_{02}^-) \\ \frac{dJ_{23}^-}{dt} &= -2i\omega_0 J_{23}^- + 2i\eta \text{Re}(a_z)(\mathcal{T}_{13}^- - \mathcal{T}_{02}^+) \\ \frac{d\mathcal{T}_{13}^-}{dt} &= -2i\omega_s \mathcal{T}_{13}^- + 2i\eta \text{Re}(a_z)(J_{23}^- - J_{01}^+) \\ \frac{d\mathcal{T}_{02}^-}{dt} &= -2i\omega_s \mathcal{T}_{02}^- + 2i\eta \text{Re}(a_z)(J_{23}^+ - J_{01}^-). \end{aligned} \tag{D4}$$

These equations result in the following precession frequencies

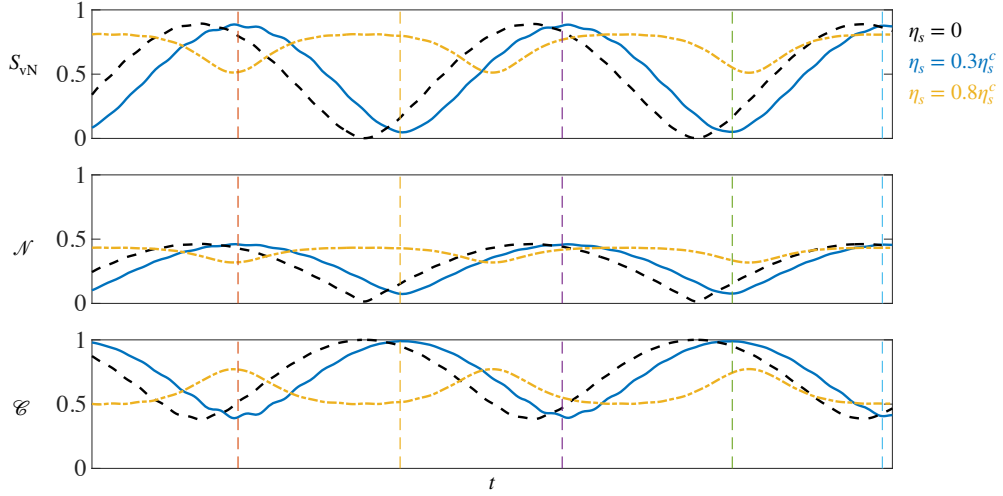


FIG. 9. Dynamics of (a) entanglement entropy S_{vN} , (b) negativity \mathcal{N} , and (c) concurrence \mathcal{C} for parameters as in Fig. 7 in the main text. Different lines correspond to different values of coupling η_s . The vertical dashed lines added to guide the eye and show the time moments when the entropy measures for $\eta_s = 0.3\eta_s^c$ case take extremal values during dynamics.

$$\begin{aligned} \Omega &\rightarrow -\sqrt{2}\sqrt{-\frac{1}{4}\sqrt{(16\eta^2 \operatorname{Re}(a_z)^2 + 4\omega_0^2 + 4\omega_s^2)^2 - 64\omega_0^2\omega_s^2 - 4\eta^2 \operatorname{Re}(a_z)^2 - \omega_0^2 - \omega_s^2}} \\ \Omega &\rightarrow -\sqrt{2}\sqrt{\frac{1}{4}\sqrt{(16\eta^2 \operatorname{Re}(a_z)^2 + 4\omega_0^2 + 4\omega_s^2)^2 - 64\omega_0^2\omega_s^2 - 4\eta^2 \operatorname{Re}(a_z)^2 - \omega_0^2 - \omega_s^2}}. \end{aligned} \quad (\text{D5})$$

Appendix E: Spin-momentum entanglement

In this Appendix, we show how the von Neumann entropy witnesses correlations between spin and momentum. Similar calculations for the negativity [54] and concurrence [55, 56] have also been performed. In our simulations, both quantities behaved similarly for all simulations, cf. Fig. 9.

We can write down the atomic state as a superposition

$$|\psi\rangle = \alpha|0\rangle + \beta|1\rangle + \gamma|2\rangle + \delta|3\rangle, \quad (\text{E1})$$

where $\alpha = \langle c_0 \rangle$, $\beta = \langle c_1 \rangle$, $\gamma = \langle c_2 \rangle$ and $\delta = \langle c_3 \rangle$, with $|\alpha|^2 + |\beta|^2 + |\gamma|^2 + |\delta|^2 = 1$ as the total number of atoms is conserved and normalized. Rewriting states $|0\rangle, \dots, |3\rangle$ in terms of spin and momentum states, see Eq. (1), the state of the system reads

$$|\psi\rangle = \alpha|0\rangle_m \otimes |\downarrow\rangle_s + \beta|1\rangle_m \otimes |\downarrow\rangle_s + \gamma|0\rangle_m \otimes |\uparrow\rangle_s + \delta|1\rangle_m \otimes |\uparrow\rangle_s. \quad (\text{E2})$$

We now can construct a reduced density matrix by summing over the spin degree of freedom

$$\tilde{\rho} = \langle \text{spin} | \psi \rangle \langle \psi | \text{spin} \rangle \quad (\text{E3})$$

or by summing over the momentum states

$$\tilde{\rho} = \langle \text{momentum} | \psi \rangle \langle \psi | \text{momentum} \rangle. \quad (\text{E4})$$

The reduced density matrix reads

$$\tilde{\rho} = \begin{bmatrix} |\alpha|^2 + |\beta|^2 & \alpha\gamma^* + \beta\delta^* \\ \alpha^*\gamma + \beta^*\delta & |\gamma|^2 + |\delta|^2 \end{bmatrix} \quad (\text{E5})$$

and can be easily diagonalized. The eigenvalues of this reduced density matrix are

$$\lambda = \frac{1}{2} \pm \frac{1}{2} \sqrt{1 - 4(|\alpha|^2|\delta|^2 + |\beta|^2|\gamma|^2 - \alpha\beta^*\gamma^*\delta - \alpha^*\beta\gamma\delta^*)}$$

or can alternatively be rewritten in terms of spins

$$\lambda = \frac{1}{2} \pm \frac{1}{2} \sqrt{1 - 4 (S_{03}^- S_{03}^+ + S_{12}^- S_{12}^+ - J_{01}^+ J_{23}^- - J_{01}^- J_{23}^+)}.$$

When $\eta = 0$, the system always remains in the pure state as the momentum state is separable in this case; in the superradiant phase, the fraction of atoms in the excited momentum state for $m_F = 0$ is the same as the fraction of excited states for $m_F = 1$.

On the other hand, when $\eta_s = 0$, the interaction η induces entanglement between spin and momentum. The easiest way to see this is to consider the two-level case when all atoms are initially prepared in state $|0\rangle$. Then, by increasing the coupling η above its critical value, the wave function of the state becomes $\psi = \alpha |0\rangle + \delta |3\rangle = \alpha |0\rangle_m \otimes |\downarrow\rangle_s + \delta |1\rangle_m \otimes |\uparrow\rangle_s$, which is not separable in spin and momentum and, thus, is entangled. This state is maximally entangled when $\alpha = \delta = 1/\sqrt{2}$, and in terms of spin and momentum degrees of freedom, the state of the system is symmetric spin-momentum configuration.

Appendix F: Spontaneous and explicit symmetry breaking

In this Appendix, we gather arguments to elucidate the source of the non-equilibrium oscillatory phases that arise when one coupling surpasses the critical threshold while the other remains below it [cf. red and blue regions in the phase diagram in Fig. 6(a)].

Let us consider the case when $\eta_s > \eta_s^c$, i.e., the cavity mode a_y is the important mode. The SR transition in H_s appears when the corresponding \mathbb{Z}_2 symmetry of the model is broken. For the subsystem built on the momentum states (via photon mode a_y , [12]), which is described by the Hamiltonian

$$H_s = \omega_y a_y^\dagger a_y + \omega_0 (c_1^\dagger c_1 + c_3^\dagger c_3) + \eta_s (a_y + a_y^\dagger) (c_0^\dagger c_1 + c_1^\dagger c_0 + c_2^\dagger c_3 + c_3^\dagger c_2), \quad (\text{F1})$$

we have the condition

$$\begin{aligned} a_y &\rightarrow -a_y \\ (c_0^\dagger c_1 + c_1^\dagger c_0 + c_2^\dagger c_3 + c_3^\dagger c_2) &\rightarrow - (c_0^\dagger c_1 + c_1^\dagger c_0 + c_2^\dagger c_3 + c_3^\dagger c_2). \end{aligned} \quad (\text{F2})$$

The second line above corresponds to $J^x \rightarrow -J^x$ for the Dicke model. Under the corresponding transformation in Eq. (12) the bosonic part of the Hamiltonian transforms as

$$\begin{aligned} (c_0^\dagger c_1 + c_1^\dagger c_0 + c_2^\dagger c_3 + c_3^\dagger c_2) &\rightarrow (c_0^\dagger c_1 e^{i(\phi_0 - \phi_1)} + c_1^\dagger c_0 e^{i(\phi_1 - \phi_0)} + c_2^\dagger c_3 e^{i(\phi_2 - \phi_3)} + c_3^\dagger c_2 e^{i(\phi_3 - \phi_2)}) \\ &= - (c_0^\dagger c_1 + c_1^\dagger c_0 + c_2^\dagger c_3 + c_3^\dagger c_2), \end{aligned} \quad (\text{F3})$$

thus setting the constraints $e^{\pm i(\phi_1 - \phi_0)} = -1$ and $e^{\pm i(\phi_2 - \phi_3)} = -1$. These constraints bring us to the following condition on the relative phases:

$$\begin{aligned} \phi_0 - \phi_1 &= \pi \pm 2\pi n \\ \phi_2 - \phi_3 &= \pi \pm 2\pi m. \end{aligned} \quad (\text{F4})$$

As only the relative phase between two bosonic fields enters the Hamiltonian, we get two conditions for four phases. If we perform the same transformation on the second interacting term in the total Hamiltonian in Eq. (8), which reads

$$\eta (a_z + a_z^\dagger) (c_1^\dagger c_2 + c_0^\dagger c_3 + c_2^\dagger c_1 + c_3^\dagger c_0), \quad (\text{F5})$$

we find that it induces an additional phase for photon field a_z , which provokes an explicit symmetry breaking

$$\begin{aligned} \eta (a_z e^{-i\phi_z} + a_z^\dagger e^{i\phi_z}) (c_1^\dagger c_2 e^{i(\phi_1 - \phi_2)} + c_0^\dagger c_3 e^{i(\phi_0 - \phi_3)} + c_2^\dagger c_1 e^{-i(\phi_1 - \phi_2)} + c_3^\dagger c_0 e^{-i(\phi_0 - \phi_3)}) &= \\ = \eta (a_z e^{-i\phi_z} + a_z^\dagger e^{i\phi_z}) (c_1^\dagger c_2 e^{i(\phi_1 - \phi_3 - \pi)} + c_0^\dagger c_3 e^{i(\phi_1 + \pi - \phi_3)} + c_2^\dagger c_1 e^{-i(\phi_1 - \phi_3 - \pi)} + c_3^\dagger c_0 e^{-i(\phi_1 + \pi - \phi_3)}) &= \\ = -\eta (a_z e^{-i\phi_z} + a_z^\dagger e^{i\phi_z}) (c_1^\dagger c_2 e^{i(\phi_1 - \phi_3)} + c_0^\dagger c_3 e^{i(\phi_1 - \phi_3)} + c_2^\dagger c_1 e^{-i(\phi_1 - \phi_3)} + c_3^\dagger c_0 e^{-i(\phi_1 - \phi_3)}) &. \end{aligned} \quad (\text{F6})$$

One can recognize that the bosonic part gains a phase $\pm(\phi_1 - \phi_3)$ which, generally, can take an arbitrary value and cannot be immediately compensated by the phase ϕ_z . So, as soon as we turn on coupling η , we break the symmetry of the Hamiltonian. In general, to restore the symmetry at finite time T , the population of the two levels (one excited and another ground momentum states) must reach zero value. In practice, when $\omega_s > 0$, particles from levels $|2\rangle$ and $|3\rangle$ drift to states $|0\rangle$ and $|1\rangle$ (or in the opposite direction when $\omega_s < 0$).

The breaking of the symmetry can be seen also in the following calculation. Given the steady state for $\eta_s > \eta_s^c$ and $\eta = 0$ [cf. Eq. (D3)], after quenching η , the photon mode a_z becomes

$$a_z = -2 \frac{\eta(\omega_z - i\kappa)}{(\omega_z^2 + \kappa^2)} \left(\sqrt{(1-\mu)\mu(1+2J^z)(1-2J^z)} \right) \quad (\text{F7})$$

which is non-zero for $\mu \neq 0, 1$. Here, the typical time at which the photon approaches the value above is $\approx 1/\kappa$ negligibly small. The explicit breaking of the symmetry in the term

$$\begin{aligned} & \eta (a_z + a_z^\dagger) \left(c_1^\dagger c_2 + c_0^\dagger c_3 + c_2^\dagger c_1 + c_3^\dagger c_0 \right) \rightarrow \\ & -\eta (a_z e^{-i\phi_z} + a_z^\dagger e^{i\phi_z}) \left(c_1^\dagger c_2 e^{i(\phi_1 - \phi_3)} + c_0^\dagger c_3 e^{i(\phi_1 - \phi_3)} + c_2^\dagger c_1 e^{-i(\phi_1 - \phi_3)} + c_3^\dagger c_0 e^{-i(\phi_1 - \phi_3)} \right) \end{aligned} \quad (\text{F8})$$

takes the system out of equilibrium. To reach steady state, the Hamiltonian must regain the symmetry via one of two mechanisms:

1. The decay of the photon number of the auxiliary mode to zero, $n_z = 0$.
2. The phases of the bosons adjusting to satisfy the condition $\phi_1 - \phi_3 \equiv 0$.

The oscillatory phase accompanies the system's dynamics until one of these two possibilities is realized. Below, we discuss both scenarios in more detail.

Appendix G: Relaxation dynamics at late times

In this Appendix, we study the properties of the system at late times and evaluate the time T at which the system restores its symmetry.

To restore the explicitly broken symmetry one needs to tune the emergent phases in front of the auxiliary photons, ϕ_c , and pseudo-spins, $\phi_i - \phi_j$, to zero. This procedure can be trivially done when the corresponding occupation of the photon or atomic levels equals zero due to the ambiguity of the phase of these complex numbers when their magnitude is zero. In the former case, the symmetry restoration occurs asymptotically at time $T \rightarrow \infty$ through the slow decay of the cavity photon magnitude induced by the dissipation κ . In line with this scenario, the dynamics, when expressed in terms of the two cavity fields, resemble the behavior depicted in the middle panels of Fig. 6(c-d) during the course of the experiment.

According to the second mechanism, which takes a finite time T , during dynamics all particles slowly transfer to the lowest energy pair of ground and excited momentum states. For instance, if $\omega_s > 0$, all particles will redistribute to levels $|0\rangle$ and $|1\rangle$ resulting into $\langle c_2(T) \rangle = 0$ and $\langle c_3(T) \rangle = 0$. Then, when states with higher energy become empty, the explicitly broken symmetry of the system can be restored. Eventually, the phases of both cavity fields remain constant, and both fields start approaching true superradiant states with $n_y \neq 0$ and $n_z \neq 0$, cf. the right panels in Fig. 6(c-d).

Fig. 10 shows the scaling of the relaxation time with (a) the fraction of particles at $t = 0$ in state $|0\rangle$, and (b) with the strength of the smaller of the two couplings, i.e, auxiliary one. Here, we prepare the system in the superradiant steady state with $\eta_s > \eta_s^c$, and then rapidly ramp the second coupling η . In these simulations we consider the mode a_z as the auxiliary one for simplicity because its critical coupling depends on μ . The finite time T corresponds to the scenario when symmetry restoration takes place through the transferring of all particles to the lower energy pair of ground and excited momentum states. For instance, for $\omega_s > 0$, the more particles are initially prepared in state $|2\rangle$, the longer is T [cf. Fig. 10(a)]. Assuming that the speed of particles transferring from levels $|2\rangle$ and $|3\rangle$ remains constant and depends solely on the couplings and detunings, the relaxation time will be proportional to the population of the zero momentum state with the higher energy. One would estimate in this case $T \propto (1 - \mu)$ as we confirm numerically in panel (a). At the same time, when $\omega_s < 0$, the pair of states that have smaller energy are $|2\rangle$ and $|1\rangle$, and the relaxation time scales like $T \propto \mu$. This can also be seen from the Hamiltonian H_{tot} which in the normal state is invariant under the transformation $\mu \leftrightarrow 1 - \mu$ when $\omega_s \rightarrow -\omega_s$.

On the other hand, the symmetry restoration time scales with the coupling to the auxiliary mode [η in Fig. 10(b)] like $T \propto \exp(-\eta)$. It means that the closer this auxiliary coupling is to its critical value, the faster the symmetry

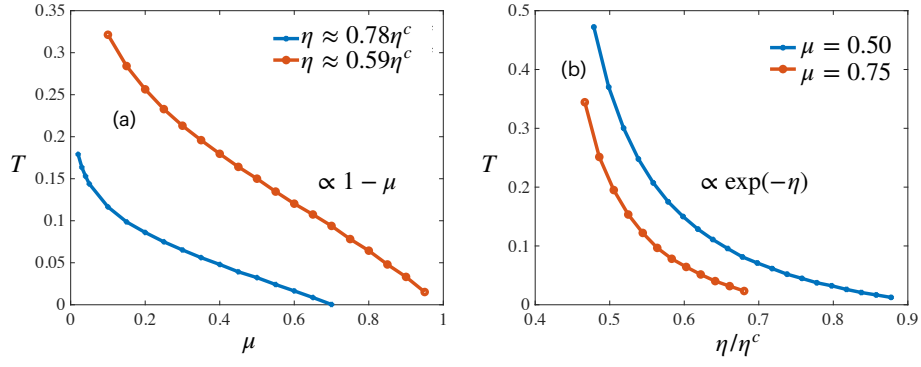


FIG. 10. Symmetry restoration time T (in seconds) as a function of (a) the initial population of the level $|0\rangle$, i.e., $N_0 = \mu N$ and (b) of the photon-matter coupling to the auxiliary cavity field. Here we consider mode a_y as the main and mode a_z as the auxiliary. Here, for simplicity, we set $\omega_y = \omega_z \approx \kappa/3$, $\omega_s = 0.2$. For these two simulations, we prepare the system in the superradiant phase for $\eta_s = 1.2\eta_s^c$, and then perform a fast ramp of $\eta < \eta^c$.

is restored. Consequently, operating within a parameter regime where the coupling to the auxiliary mode remains significantly below the critical threshold, yet remains finite, gives us the opportunity to probe the atomic dynamics within the system with minimal disruption.

Below we consider a few fine-tuned limits in which a stationary state can not be reached within the operational timescales of the experiment.

1. $\kappa/\omega_c \rightarrow \infty$ limit

The relaxation time T depends on the strength of the photon-matter coupling with the auxiliary mode; namely, the stronger the interaction, the faster the relaxation [see Fig. 10(b)]. On the other hand, the strength of this coupling controls the population of the auxiliary cavity mode, $n \propto \eta^2/(\omega_c^2 + \kappa^2)$. As such, it is instructive to explore the regime where $\eta/\sqrt{\omega_c^2 + \kappa^2}$ is large enough to produce sufficiently large cavity field amplitude to enable detections of oscillations in the auxiliary cavity field. We would also like to simultaneously satisfy the condition $\eta \ll \eta_c$ so that the system's restoration of its symmetry becomes protracted to exponentially late times. These conditions can be satisfied simultaneously when $\omega_c \ll \kappa$, a regime in which the critical coupling diverges like $\sqrt{\omega_0 \kappa^2/\omega_c}$. The extreme case of $\omega_c = 0$ corresponds to the critical coupling tending to infinity. Counter-intuitively, in this case, one enters a strong dissipation regime which prevents the relaxation.

The main idea of why the strong dissipation regime prevents relaxation can be explained as follows: according to the Hamiltonian H_{tot} [Eq. (8)], pseudo-spins are coupled to the real quadrature of the cavity fields, $a + a^\dagger$. If the cavity fields are coupled to the x -components of pseudo-spins, then the cavity field is imaginary, $a_y \propto 2J^x/(-i\kappa)$ (or $a_z \propto 2S^x/(-i\kappa)$). Here the cavity decay rate causes a phase shift $\phi_\kappa^{y,z} = \tan^{-1}(-\kappa/\omega_{y,z})$ of the field scattered into the cavity by the atomic system [11]. Thus, by setting the cavity detuning ω_y or ω_z to be much smaller than κ , one can make the corresponding cavity field imaginary and eliminate its feedback on the spin dynamics. For instance, when $\eta_s > \eta_s^c$, $\eta < \eta^c$ and $\omega_y \neq 0$, $\omega_z \rightarrow 0$ [blue region in Fig. 6(a)], a_y approaches its steady state value, while $a_z \approx -2\eta(S_{03}^x + S_{12}^x)/(-i\kappa)$ oscillates together with the precession of the pseudo-spin S^x . However, as $(a_z + a_z^\dagger) \rightarrow 0$, the non-stationary behavior of the cavity field does not impact the dynamics of pseudo-spin S^x . In other words, subsystem H_s constantly induces precession for pseudo-spin S^x (and thus oscillations to the cavity mode a_z) due to the explicit symmetry breaking; it does not, however, experience feedback from subsystem H . As a result, the lack of reciprocal interaction between the two subsystems prevents the system from reaching a steady state, and oscillations in the auxiliary cavity mode a_z survive for an arbitrarily long time.

When $\eta_s < \eta_s^c$ and $\eta > \eta^c$ [red region in the phase diagram in Fig. 6(a)], one should set $\omega_y \ll \kappa$ to prevent the system from reaching its steady state. In this case, the cavity mode a_y will exhibit oscillations around zero for an arbitrarily long time, reflecting the precession of pseudo-spin J^x . The cavity mode a_z , in turn, will approach its steady state value, determined solely by the Hamiltonian H [Eq. (2)] and initial conditions.

Interestingly, in the opposite limit where $\omega_c \gg \kappa$, the system can also experience slow relaxation. The critical coupling scales like $\eta_c \propto \sqrt{\omega_0 \omega_c} \rightarrow \infty$; it is easier to keep the coupling strongly subcritical while still large enough to enable read-out. However, as the cavity occupation scales as $n \propto 1/\omega_c^2$, in order to keep n non-zero, it is essential to keep the cavity detuning finite.

2. $\omega_s \rightarrow 0$ limit

One can recognize from the level scheme in Fig. 2(b) that when $\omega_s = 0$, the two ground states in the momentum variables, $|0\rangle, |2\rangle$, and the two excited ones $|1\rangle, |3\rangle$ are degenerate. In this case, the Hamiltonian acquires an additional symmetry under exchange between ground or excited states, namely $c_1 \leftrightarrow c_3, c_0 \leftrightarrow c_2$ (see Hamiltonian in the bosonic representation in Appendix A). As a consequence, the dynamics for the pair of fields c_1, c_3 (and likewise for c_0, c_2) occur at the same frequencies $c_1, c_3 \propto \exp(i\Omega t)$. Accordingly, the phase that explicitly breaks the symmetry of the Hamiltonian, $\pm(\phi_1 - \phi_3)$, remains constant over time, determined solely by the initial conditions (which can be arbitrary and are not restricted in general). Thus, after the quench, both spins J^x and S^x gain fixed time values, and one can observe superradiance in both cavity modes simultaneously. Interestingly, in this case, n_y and n_z do not oscillate over time, and non-stationary behavior can only be observed at the level of the atomic observables. In particular, particles redistribute between different excited or ground momentum states so that the overall number of particles in the upper and lower spinor components oscillates over time around a common time-averaged value.

Appendix H: Three-level model

We now revisit the possibility of probing the system's dynamics with the auxiliary cavity field in a three-level system. As mentioned in the main text, such a model includes single ground momentum state $|2\rangle$, and two excited momentum states $|1\rangle, |3\rangle$, where we keep notation as in the Eq. (1). Such Hamiltonian can be implemented when fixing $\mathbf{e}_p = \mathbf{e}_x$ in Eq. (A7) and considering resonant spin changing and spin-dependent processes, cf. implementations in Refs. [11, 36]. Here we omit the implementation of the three-level model, concentrating mostly on the physical phenomena, compared to the four-level model in Eq. (8). To do so, we study the effect of spontaneous symmetry breaking in one sector of the Hamiltonian on the dynamical properties in another sector. As we demonstrate below, explicit symmetry breaking in the self-ordered phase(s) is not pronounced in the three-level case, thereby resulting in trivial system dynamics.

The Hamiltonian of our three-level model reads

$$H_3 = \omega_y a_y^\dagger a_y + \omega_z a_z^\dagger a_z + \omega_0 (c_1^\dagger c_1 + c_3^\dagger c_3) + \omega_s (c_2^\dagger c_2 + c_3^\dagger c_3) + \eta (a_z + a_z^\dagger) (c_1^\dagger c_2 + c_2^\dagger c_1) + \eta_s (a_y + a_y^\dagger) (c_2^\dagger c_3 + c_3^\dagger c_2). \quad (\text{H1})$$

Let us consider the effect of the spontaneous symmetry breaking in one subsystem on the dynamics of another, similarly as it is done in Appendix F. Firstly, we consider a steady state when $\eta_s > \eta_s^c$ and $\eta = 0$. In this case, the symmetry of a subsystem involving photon mode a_y is broken, meaning there exist two solutions, satisfying

$$a_y \rightarrow -a_y \\ (c_2^\dagger c_3 + c_3^\dagger c_2) \rightarrow - (c_2^\dagger c_3 + c_3^\dagger c_2). \quad (\text{H2})$$

Applying transformation (12), we can see that such transformation

$$(c_2^\dagger c_3 + c_3^\dagger c_2) \rightarrow (c_2^\dagger c_3 e^{i(\phi_2 - \phi_3)} + c_3^\dagger c_2 e^{i(\phi_3 - \phi_2)}) \\ = - (c_2^\dagger c_3 + c_3^\dagger c_2) \quad (\text{H3})$$

sets the following constraints on relative phases

$$\phi_2 - \phi_3 = \pi \pm 2\pi m. \quad (\text{H4})$$

Note that there are no restrictions on the phase ϕ_1 because photon mode a_y is not coupled to the level $|1\rangle$. As such, making the second coupling, η , non-zero does not induce explicit symmetry breaking. This fact can be seen by applying the transformation (12) to this term:

$$(a_z e^{-i\phi_z} + a_z^\dagger e^{i\phi_z}) (c_1^\dagger c_2 e^{i(\phi_1 - \phi_2)} + c_2^\dagger c_1 e^{-i(\phi_1 - \phi_2)}) \propto \langle c_1 \rangle \equiv 0. \quad (\text{H5})$$

The phase of the boson field c_1 can always compensate for the restricted phase of c_2 . Note that we assume that level $|1\rangle$ is unoccupied before increasing η , and thus the phase of c_1 can be changed arbitrarily. The system is therefore

stable against quenches $\eta < \eta^c$. This behavior arises from the fact that each photon mode is not coupled to all atomic levels; symmetry breaking in one interaction term does not imply explicit symmetry breaking in another. More precisely, when $\eta_s > \eta_s^c$ and $\eta = 0$, one finds that

$$\begin{aligned} c_1^\dagger c_1 &= 0 \\ c_2^\dagger c_2 &= \frac{(1 - 2J^z)}{2} \\ c_3^\dagger c_3 &= \frac{(1 + 2J_z)}{2} \end{aligned} \tag{H6}$$

and after the quench of η , we get $a_z \propto (c_1^\dagger c_2 + c_2^\dagger c_1) = 0$ and the subsystem remains in steady state as long as $\eta/\eta^c < \eta_s/\eta_s^c$. The absence of restrictions on phase ϕ_1 makes it impossible to induce competing conditions and push the subsystem out of equilibrium. Indeed, in the case of four levels, one cannot manipulate the phase of a single boson separately, thereby resulting in the existence of long-lived oscillations of the auxiliary cavity field and the precession of corresponding pseudo-spins.

-
- [1] Jun John Sakurai and Eugene D Commins, “Modern quantum mechanics, revised edition,” (1995).
- [2] J. E. Hirsch, “Spin hall effect,” *Phys. Rev. Lett.* **83**, 1834–1837 (1999).
- [3] M. Z. Hasan and C. L. Kane, “Colloquium: Topological insulators,” *Rev. Mod. Phys.* **82**, 3045–3067 (2010).
- [4] Masatoshi Sato and Yoichi Ando, “Topological superconductors: a review,” *Reports on Progress in Physics* **80**, 076501 (2017).
- [5] Jay D. Sau, Roman M. Lutchyn, Sumanta Tewari, and S. Das Sarma, “Generic new platform for topological quantum computation using semiconductor heterostructures,” *Phys. Rev. Lett.* **104**, 040502 (2010).
- [6] Jiaan Qi, Zhi-Hai Liu, and HQ Xu, “Spin-orbit interaction enabled high-fidelity two-qubit gates,” arXiv preprint arXiv:2308.06986 (2023).
- [7] Tomer Stav, Arkady Faerman, Elhanan Maguid, Dikla Oren, Vladimir Kleiner, Erez Hasman, and Mordechai Segev, “Quantum entanglement of the spin and orbital angular momentum of photons using metamaterials,” *Science* **361**, 1101–1104 (2018), <https://www.science.org/doi/pdf/10.1126/science.aat9042>.
- [8] Sumit Suresh Kale, Yijue Ding, Yong P Chen, Bretislav Friedrich, and Sabre Kais, “Spin-momentum entanglement in a bose–einstein condensate,” *Physical Chemistry Chemical Physics* **22**, 25669–25674 (2020).
- [9] Marco T Manzoni, Ludwig Mathey, and Darrick E Chang, “Designing exotic many-body states of atomic spin and motion in photonic crystals,” *Nature communications* **8**, 14696 (2017).
- [10] Farokh Mivehvar, Francesco Piazza, Tobias Donner, and Helmut Ritsch, “Cavity qed with quantum gases: new paradigms in many-body physics,” *Advances in Physics* **70**, 1–153 (2021).
- [11] Nishant Dogra, Manuele Landini, Katrin Kroeger, Lorenz Hruby, Tobias Donner, and Tilman Esslinger, “Dissipation-induced structural instability and chiral dynamics in a quantum gas,” *Science* **366**, 1496–1499 (2019).
- [12] Kristian Baumann, Christine Guerlin, Ferdinand Brennecke, and Tilman Esslinger, “Dicke quantum phase transition with a superfluid gas in an optical cavity,” *nature* **464**, 1301–1306 (2010).
- [13] Ronen M. Kroeze, Yudan Guo, and Benjamin L. Lev, “Dynamical spin-orbit coupling of a quantum gas,” *Phys. Rev. Lett.* **123**, 160404 (2019).
- [14] Jamir Marino, Martin Eckstein, Matthew Foster, and Ana-Maria Rey, “Dynamical phase transitions in the collisionless pre-thermal states of isolated quantum systems: theory and experiments,” *Reports on Progress in Physics* (2022).
- [15] Jens Klinder, Hans Keßler, Matthias Wolke, Ludwig Mathey, and Andreas Hemmerich, “Dynamical phase transition in the open dicke model,” *Proceedings of the National Academy of Sciences* **112**, 3290–3295 (2015), <https://www.pnas.org/doi/pdf/10.1073/pnas.1417132112>.
- [16] Jim Skulte, Phatthamon Kongkhambut, Hans Keßler, Andreas Hemmerich, Ludwig Mathey, and Jayson G. Cosme, “Parametrically driven dissipative three-level dicke model,” *Phys. Rev. A* **104**, 063705 (2021).
- [17] Phatthamon Kongkhambut, Hans Keßler, Jim Skulte, Ludwig Mathey, Jayson G. Cosme, and Andreas Hemmerich, “Realization of a periodically driven open three-level dicke model,” *Phys. Rev. Lett.* **127**, 253601 (2021).
- [18] Phatthamon Kongkhambut, Jim Skulte, Ludwig Mathey, Jayson G. Cosme, Andreas Hemmerich, and Hans Keßler, “Observation of a continuous time crystal,” *Science* **377**, 670–673 (2022), <https://www.science.org/doi/pdf/10.1126/science.abo3382>.
- [19] Robert J. Lewis-Swan, Diego Barberena, Julia R. K. Cline, Dylan J. Young, James K. Thompson, and Ana Maria Rey, “Cavity-qed quantum simulator of dynamical phases of a bardeen-cooper-schrieffer superconductor,” *Phys. Rev. Lett.* **126**, 173601 (2021).
- [20] Federico Carollo and Igor Lesanovsky, “Exactness of mean-field equations for open dicke models with an application to pattern retrieval dynamics,” *Phys. Rev. Lett.* **126**, 230601 (2021).
- [21] K. Seetharam, A. Leroze, R. Fazio, and J. Marino, “Correlation engineering via nonlocal dissipation,” *Phys. Rev.*

- Res.* **4**, 013089 (2022).
- [22] K. Seetharam, A. Lerose, R. Fazio, and J. Marino, “Dynamical scaling of correlations generated by short- and long-range dissipation,” *Phys. Rev. B* **105**, 184305 (2022).
- [23] Jamir Marino, “Universality class of ising critical states with long-range losses,” *Phys. Rev. Lett.* **129**, 050603 (2022).
- [24] Avikar Periwal, Eric S Cooper, Philipp Kunkel, Julian F Wienand, Emily J Davis, and Monika Schleier-Smith, “Programmable interactions and emergent geometry in an array of atom clouds,” *Nature* **600**, 630–635 (2021).
- [25] Fabian Finger, Rodrigo Rosa-Medina, Nicola Reiter, Panagiotis Christodoulou, Tobias Donner, and Tilman Esslinger, “Spin- and momentum-correlated atom pairs mediated by photon exchange,” (2023), [arXiv:2303.11326 \[cond-mat.quant-gas\]](https://arxiv.org/abs/2303.11326).
- [26] Rodrigo Rosa-Medina, Francesco Ferri, Fabian Finger, Nishant Dogra, Katrin Kroeger, Rui Lin, R. Chitra, Tobias Donner, and Tilman Esslinger, “Observing dynamical currents in a non-hermitian momentum lattice,” *Phys. Rev. Lett.* **128**, 143602 (2022).
- [27] Rui Lin, Rodrigo Rosa-Medina, Francesco Ferri, Fabian Finger, Katrin Kroeger, Tobias Donner, Tilman Esslinger, and R. Chitra, “Dissipation-engineered family of nearly dark states in many-body cavity-atom systems,” *Phys. Rev. Lett.* **128**, 153601 (2022).
- [28] Jim Skulte, Phatthamon Kongkhambut, Sahana Rao, Ludwig Mathey, Hans Keßler, Andreas Hemmerich, and Jayson G. Cosme, “Condensate formation in a dark state of a driven atom-cavity system,” *Phys. Rev. Lett.* **130**, 163603 (2023).
- [29] A. Piñeiro Orioli, J. K. Thompson, and A. M. Rey, “Emergent dark states from superradiant dynamics in multilevel atoms in a cavity,” *Phys. Rev. X* **12**, 011054 (2022).
- [30] M. Soriente, T. Donner, R. Chitra, and O. Zilberberg, “Dissipation-induced anomalous multicritical phenomena,” *Phys. Rev. Lett.* **120**, 183603 (2018).
- [31] Manuele Landini, Nishant Dogra, Katrin Kröger, Lorenz Hruby, Tobias Donner, and Tilman Esslinger, “Formation of a spin texture in a quantum gas coupled to a cavity,” *Physical review letters* **120**, 223602 (2018).
- [32] Davide Dreon, Alexander Baumgärtner, Xiangliang Li, Simon Hertlein, Tilman Esslinger, and Tobias Donner, “Self-oscillating pump in a topological dissipative atom-cavity system,” *Nature* **608**, 494–498 (2022).
- [33] D. Nagy, G. Kónya, G. Szirmai, and P. Domokos, “Dicke-model phase transition in the quantum motion of a bose-einstein condensate in an optical cavity,” *Phys. Rev. Lett.* **104**, 130401 (2010).
- [34] Zhang Zhiqiang, Chern Hui Lee, Ravi Kumar, KJ Arnold, Stuart J Masson, AS Parkins, and MD Barrett, “Nonequilibrium phase transition in a spin-1 dicke model,” *Optica* **4**, 424–429 (2017).
- [35] Stuart J. Masson, M. D. Barrett, and Scott Parkins, “Cavity qed engineering of spin dynamics and squeezing in a spinor gas,” *Phys. Rev. Lett.* **119**, 213601 (2017).
- [36] Francesco Ferri, Rodrigo Rosa-Medina, Fabian Finger, Nishant Dogra, Matteo Soriente, Oded Zilberberg, Tobias Donner, and Tilman Esslinger, “Emerging dissipative phases in a superradiant quantum gas with tunable decay,” *Phys. Rev. X* **11**, 041046 (2021).
- [37] Ronen M. Kroeze, Yudan Guo, Varun D. Vaidya, Jonathan Keeling, and Benjamin L. Lev, “Spinor self-ordering of a quantum gas in a cavity,” *Phys. Rev. Lett.* **121**, 163601 (2018).
- [38] Farokh Mivehvar, Francesco Piazza, and Helmut Ritsch, “Disorder-driven density and spin self-ordering of a bose-einstein condensate in a cavity,” *Phys. Rev. Lett.* **119**, 063602 (2017).
- [39] John Drew Wilson, Simon B. Jäger, Jarrod T. Reilly, Athreya Shankar, Maria Luisa Chiofalo, and Murray J. Holland, “Beyond one-axis twisting: Simultaneous spin-momentum squeezing,” *Phys. Rev. A* **106**, 043711 (2022).
- [40] D. Nagy, G. Szirmai, and P. Domokos, “Critical exponent of a quantum-noise-driven phase transition: The open-system dicke model,” *Phys. Rev. A* **84**, 043637 (2011).
- [41] Kevin C. Stitely, Andrus Giraldo, Bernd Krauskopf, and Scott Parkins, “Lasing and counter-lasing phase transitions in a cavity-qed system,” *Phys. Rev. Res.* **4**, 023101 (2022).
- [42] Alessio Lerose and Silvia Pappalardi, “Bridging entanglement dynamics and chaos in semiclassical systems,” *Phys. Rev. A* **102**, 032404 (2020).
- [43] Nicolò Defenu, Alessio Lerose, and Silvia Pappalardi, “Out-of-equilibrium dynamics of quantum many-body systems with long-range interactions,” (2023), [arXiv:2307.04802 \[cond-mat.quant-gas\]](https://arxiv.org/abs/2307.04802).
- [44] Peter Kirton, Mor M Roses, Jonathan Keeling, and Emanuele G Dalla Torre, “Introduction to the dicke model: From equilibrium to nonequilibrium, and vice versa,” *Advanced Quantum Technologies* **2**, 1800043 (2019).
- [45] Michael A. Nielsen and Isaac L. Chuang, *Quantum Computation and Quantum Information: 10th Anniversary Edition* (Cambridge University Press, 2010).
- [46] Zhiqiang Zhang, Chern Hui Lee, Ravi Kumar, K. J. Arnold, Stuart J. Masson, A. L. Grimsmo, A. S. Parkins, and M. D. Barrett, “Dicke-model simulation via cavity-assisted raman transitions,” *Phys. Rev. A* **97**, 043858 (2018).
- [47] Oksana Chelpanova, Alessio Lerose, Shu Zhang, Iacopo Carusotto, Yaroslav Tserkovnyak, and Jamir Marino, “Intertwining of lasing and superradiance under spintronic pumping,” *Phys. Rev. B* **108**, 104302 (2023).
- [48] R. H. Dicke, “Coherence in spontaneous radiation processes,” *Phys. Rev.* **93**, 99–110 (1954).
- [49] F. Dimer, B. Estienne, A. S. Parkins, and H. J. Carmichael, “Proposed realization of the dicke-model quantum phase transition in an optical cavity qed system,” *Phys. Rev. A* **75**, 013804 (2007).
- [50] Peter Kirton and Jonathan Keeling, “Superradiant and lasing states in driven-dissipative dicke models,” *New Journal of Physics* **20**, 015009 (2018).
- [51] Farokh Mivehvar, “Unconventional dicke model: Multistabilities and nonequilibrium dynamics,” (2023), [arXiv:2307.05686 \[quant-ph\]](https://arxiv.org/abs/2307.05686).
- [52] Brendan P Marsh, Ronen M Kroeze, Surya Ganguli, Sarang Gopalakrishnan, Jonathan Keeling, and Benjamin L Lev, “Entanglement and replica symmetry breaking in a driven-dissipative quantum spin glass,” *arXiv preprint arXiv:2307.10176* (2023).
- [53] Farokh Mivehvar, Helmut Ritsch, and Francesco Piazza, “Cavity-quantum-electrodynamical toolbox for quantum magnetism,” *Phys. Rev. Lett.* **122**, 113603 (2019).
- [54] Eyal Cornfeld, Moshe Goldstein, and Eran Sela, “Im-

- balance entanglement: Symmetry decomposition of negativity,” *Phys. Rev. A* **98**, 032302 (2018).
- [55] William K Wootters, “Entanglement of formation and concurrence.” *Quantum Inf. Comput.* **1**, 27–44 (2001).
- [56] Ji Zou, Shu Zhang, and Yaroslav Tserkovnyak, “Bell-state generation for spin qubits via dissipative coupling,” *Physical Review B* **106** (2022), [10.1103/physrevb.106.1180406](https://doi.org/10.1103/physrevb.106.1180406).
- [57] G. Vidal and R. F. Werner, “Computable measure of entanglement,” *Phys. Rev. A* **65**, 032314 (2002).
- [58] Dolf Huybrechts, Fabrizio Minganti, Franco Nori, Michiel Wouters, and Nathan Shammah, “Validity of mean-field theory in a dissipative critical system: Liouvillian gap, $\mathbb{P}\mathbb{T}$ -symmetric antigap, and permutational symmetry in the XYZ model,” *Phys. Rev. B* **101**, 214302 (2020).
- [59] Zihao Qi, Thomas Scaffidi, and Xiangyu Cao, “Surprises in the deep hilbert space of all-to-all systems: From superexponential scrambling to slow entanglement growth,” *Phys. Rev. B* **108**, 054301 (2023).
- [60] Fernando Iemini, Darrick Chang, and Jamir Marino, “Dynamics of inhomogeneous spin ensembles with all-to-all interactions: breaking permutational invariance,” (2023), [arXiv:2309.10746 \[quant-ph\]](https://arxiv.org/abs/2309.10746).
- [61] Riccardo J. Valencia-Tortora, Shane P. Kelly, Tobias Donner, Giovanna Morigi, Rosario Fazio, and Jamir Marino, “Crafting the dynamical structure of synchronization by harnessing bosonic multilevel cavity qed,” *Phys. Rev. Res.* **5**, 023112 (2023).
- [62] Victor Galitski and Ian B Spielman, “Spin-orbit coupling in quantum gases,” *Nature* **494**, 49–54 (2013).
- [63] Salvatore Lorenzo, Jamir Marino, Francesco Plastina, G Massimo Palma, and Tony JG Apollaro, “Quantum critical scaling under periodic driving,” *Scientific reports* **7**, 5672 (2017).
- [64] Stuart S. Szigeti, Onur Hosten, and Simon A. Haine, “Improving cold-atom sensors with quantum entanglement: Prospects and challenges,” *Applied Physics Letters* **118**, 140501 (2021), https://pubs.aip.org/aip/apl/article-pdf/doi/10.1063/5.0050235/14546135/140501_1.online.pdf.
- [65] Simone Colombo, Edwin Pedrozo-Peñafiel, and Vladan Vuletić, “Entanglement-enhanced optical atomic clocks,” *Applied Physics Letters* **121** (2022).
- [66] Graham P Greve, Chengyi Luo, Baochen Wu, and James K Thompson, “Entanglement-enhanced matter-wave interferometry in a high-finesse cavity,” *Nature* **610**, 472–477 (2022).
- [67] Ferdinand Brennecke, Rafael Mottl, Kristian Baumann, Renate Landig, Tobias Donner, and Tilman Esslinger, “Real-time observation of fluctuations at the driven-dissipative dicke phase transition,” *Proceedings of the National Academy of Sciences* **110**, 11763–11767 (2013), <https://www.pnas.org/doi/pdf/10.1073/pnas.1306993110>.
- [68] M. J. Bhaseen, J. Mayoh, B. D. Simons, and J. Keeling, “Dynamics of nonequilibrium dicke models,” *Phys. Rev. A* **85**, 013817 (2012).
- [69] We also tried sampling various initial states and comparing dynamics. Our general observation is the oscillatory behavior is quite generic and repeats from simulation to simulation. However, the frequency of oscillations may depend on the initial state.
- [70] François Damanet, Andrew J. Daley, and Jonathan Keeling, “Atom-only descriptions of the driven-dissipative dicke model,” *Phys. Rev. A* **99**, 033845 (2019).
- [71] Simon B. Jäger, Tom Schmit, Giovanna Morigi, Murray J. Holland, and Ralf Betzholz, “Lindblad master equations for quantum systems coupled to dissipative bosonic modes,” *Phys. Rev. Lett.* **129**, 063601 (2022).
- [72] J. Keeling, M. J. Bhaseen, and B. D. Simons, “Collective dynamics of bose-einstein condensates in optical cavities,” *Phys. Rev. Lett.* **105**, 043001 (2010).
- [73] Tanmay Bhore, Jean-Yves Desaulles, and Zlatko Papić, “Deep thermalization in constrained quantum systems,” (2023), [arXiv:2307.03769 \[quant-ph\]](https://arxiv.org/abs/2307.03769).
- [74] Riccardo J. Valencia-Tortora, Nicola Pancotti, and Jamir Marino, “Kinetically constrained quantum dynamics in superconducting circuits,” *PRX Quantum* **3**, 020346 (2022).
- [75] A Piñeiro Orioli and AM Rey, “Subradiance of multilevel fermionic atoms in arrays with filling $n \geq 2$,” *Physical Review A* **101**, 043816 (2020).
- [76] Christoph Hotter, Laurin Ostermann, and Helmut Ritsch, “Cavity sub- and superradiance for transversely driven atomic ensembles,” *Phys. Rev. Res.* **5**, 013056 (2023).
- [77] Bhuvanesh Sundar, Diego Barberena, Ana Maria Rey, and Asier Pineiro Orioli, “Squeezing multilevel atoms in dark states via cavity superradiance,” *arXiv preprint arXiv:2302.10828* (2023).
- [78] Ana Asenjo-Garcia, HJ Kimble, and Darrick E Chang, “Optical waveguiding by atomic entanglement in multilevel atom arrays,” *Proceedings of the National Academy of Sciences* **116**, 25503–25511 (2019).
- [79] Stuart J Masson and Ana Asenjo-Garcia, “Universality of dicke superradiance in arrays of quantum emitters,” *Nature Communications* **13**, 2285 (2022).
- [80] Eric Sierra, Stuart J Masson, and Ana Asenjo-Garcia, “Dicke superradiance in ordered lattices: dimensionality matters,” *Physical Review Research* **4**, 023207 (2022).
- [81] C. Tabares, A. Muñoz de las Heras, L. Tagliacozzo, D. Porras, and A. González-Tudela, “Variational quantum simulators based on waveguide qed,” *Phys. Rev. Lett.* **131**, 073602 (2023).
- [82] Jarrod T. Reilly, Simon B. Jäger, John Drew Wilson, John Cooper, Sebastian Eggert, and Murray J. Holland, “Speeding up squeezing with a periodically driven dicke model,” (2023), [arXiv:2310.07694 \[quant-ph\]](https://arxiv.org/abs/2310.07694).
- [83] Berislav Buča and Dieter Jaksch, “Dissipation induced nonstationarity in a quantum gas,” *Physical review letters* **123**, 260401 (2019).
- [84] Rukhsan Ul Haq, Sachin Satish Bharadwaj, and Towseef Ali Wani, “An explicit method for schrieffer-wolff transformation,” (2019), [arXiv:1901.08617 \[cond-mat.str-el\]](https://arxiv.org/abs/1901.08617).
- [85] Daniel A Steck, “Rubidium 87 d line data,” (2021).
- [86] Oleg V Sinkin, Ronald Holzlöhner, John Zweck, and Curtis R Menyuk, “Optimization of the split-step fourier method in modeling optical-fiber communications systems,” *Journal of lightwave technology* **21**, 61 (2003).